Journal of Molecular Structure 1351 (2026) 144342

Contents lists available at ScienceDirect

Journal of Molecular Structure

journal homepage: www.elsevier.com/locate/molstr

Acyl thiosemicarbazides as novel inhibitors for zinc substrate in saline solution

Thu Thuy Pham [a,b], Chien Thang Pham [c,*], Hong Nhung Nguyen [c], Quang Khanh Nguyen [c,d], Anh Son Nguyen [a], David Cornil [e], Jérôme Cornil [e], Thuy Duong Nguyen [a], Alice Belfiore [f], Thi Xuan Hang To [a], Marie-Georges Olivier [b,f,*]

[a] Institute of Materials Science, Vietnam Academy of Science and Technology, 18 Hoang Quoc Viet, Cau Giay, Hanoi, Vietnam
[b] Université de Mons, Materials Science Department, Place du Parc 20, Mons, Belgium
[c] Faculty of Chemistry, VNU University of Science, Vietnam National University, Hanoi, 19 Le Thanh Tong, Hanoi, Vietnam
[d] Department of Chemistry, College of Natural Sciences, Hanyang University, Seoul, 04763, Republic of Korea
[e] Laboratory for Chemistry of Novel Materials, University of Mons (UMONS), 20 Place du Parc, Mons B-7000, Belgium
[f] Materia Nova, Parc Initialis, Mons, Belgium

ARTICLE INFO

Keywords:
Acyl thiosemicarbazides
Corrosion inhibitors
Zinc substrate

ABSTRACT

Three acyl thiosemicarbazides, namely picolinoyl N4-phenylthiosemicarbazide (**HL^1**), salicyloyl N4-phenylthiosemicarbazide (**HL^2**), and anthraniloyl N4-phenylthiosemicarbazide (**HL^3**), were synthesized and structurally characterized. Their corrosion inhibition performance on zinc substrates in 0.1 M NaCl solution was evaluated using polarization curves and electrochemical impedance spectroscopy (EIS). The interactions between the inhibitor molecules and the substrate surface, as well as the resulting corrosion products, were investigated using X-ray photoelectron spectroscopy (XPS), field-emission scanning electronic microscopy (FE-SEM), and energy dispersive X-ray spectroscopy (EDS). Density functional theory (DFT) calculations were further employed to elucidate the relationship between the electronic properties of the compounds and their inhibitor mechanism. Electrochemical measurements confirmed that **HL^1**, **HL^2**, and **HL^3** acted as mixed-type inhibitors, with a predominant effect on the anodic dissolution of zinc. The inhibition efficiency of **HL^1** significantly increased from 46.47% at 1.0×10^{-5} M to 97.22% at 1.0×10^{-3} M, while at the same concentration (1.0×10^{-3} M), **HL^3** provided the highest protection efficiency (98.59%), followed by **HL^2** (97.82%) and **HL^1**. Surface characterization and theoretical analysis revealed strong zinc-inhibitor interactions at the metal/oxide-solution interface, reflected by adhesion energy (E_{adh}) and summation of bond orders (SBO) calculations. The enhanced corrosion resistance of the zinc substrates was ascribed to the formation of zinc ion-inhibitor coordination complexes at the interface, which effectively hindered chloride ion penetration. Moreover, the superior performance of **HL^3** was rationalized by its stronger electron-donating character, as indicated by molecular electrostatic potential (MEP) and Fukui function analyses, and its stronger adhesion to oxidized zinc surfaces, supported by the most negative E_{adh} (–3.55 eV), the highest SBO (2.55), and the favorable alignment of its HOMO level with the valence band of ZnO.

1. Introduction

Zinc is an essential non-ferrous metal widely used in civil construction, the automotive sector, and various industrial applications [1]. A substantial portion of zinc and its alloys is applied for coating and galvanizing ferrous metallic articles [2]. The corrosion behavior of zinc alloys and galvanized steel has been investigated in different corrosion environments, including acidic, alkaline, near-neutral medium, and marine environments [2–5]. Previous works found that ZnO, $Zn(OH)_2$, $Zn_5(OH)_8Cl_2{\cdot}2H_2O$, and $Zn_5(OH)_6(CO_3)_2{\cdot}H_2O$ were main insoluble corrosion products of zinc after exposure to corrosive chloride-containing environments [2,5,6]. These corrosion products can accumulate on zinc surfaces and provide corrosion protection depending on their structure, morphology, solubility, and compactness [2].

* Corresponding authors.
E-mail addresses: phamchienthang@hus.edu.vn (C.T. Pham), marjorie.olivier@umons.ac.be (M.-G. Olivier).

https://doi.org/10.1016/j.molstruc.2025.144342
Received 15 June 2025; Received in revised form 8 October 2025; Accepted 9 October 2025
Available online 10 October 2025

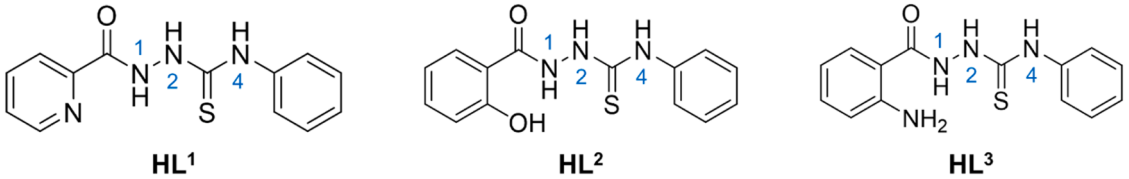

Scheme 1. Acyl thiosemicarbazides used in the present work: picolinoyl N4-phenylthiosemicarbazide (**HL^1**), salicyloyl N4-phenylthiosemicarbazide (**HL^2**), and anthraniloyl N4-phenylthiosemicarbazide (**HL^3**).

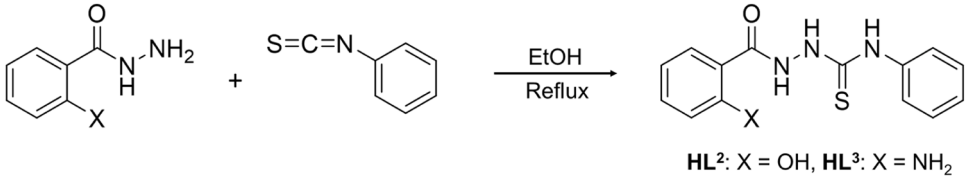

Scheme 2. Syntheses of the acyl thiosemicarbazides **HL^2** and **HL^3**.

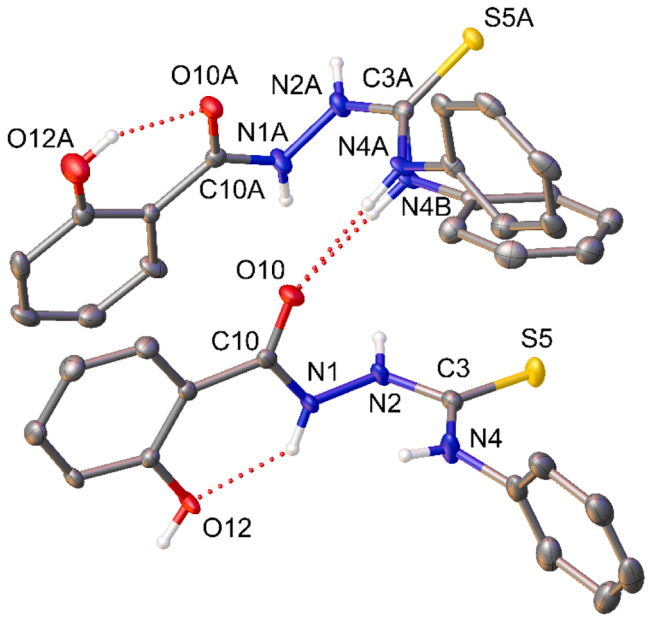

Fig. 1. Molecular structure of the asymmetric unit of **HL^2**. The dotted lines present hydrogen bonds.

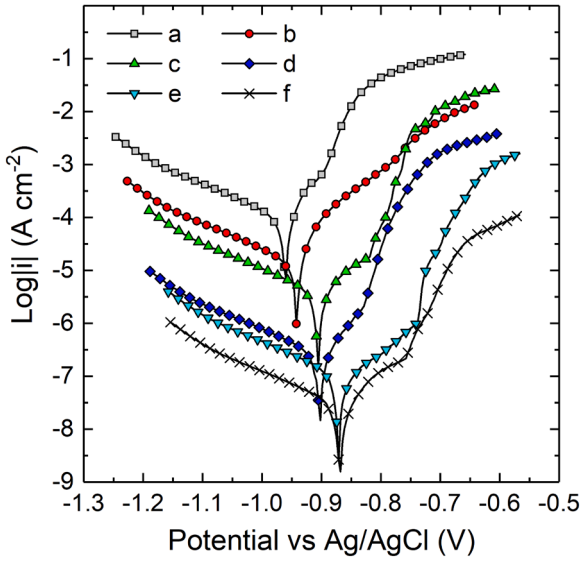

Fig. 2. Potentiodynamic polarization curves of zinc in 0.1 M NaCl solution without inhibitor (a), and with 1.0×10^{-5} M **HL^1** (b), 1.0×10^{-4} M **HL^1** (c), 1.0×10^{-3} M **HL^1** (d), 1.0×10^{-3} M **HL^2** (e), 1.0×10^{-3} M **HL^3** (f).

Table 1
Selected experimental and calculated bond lengths/ Å in **HL^2**.

Anti	Exp.	Cal.	*Syn*	Exp.	Cal.
C10–O10	1.227 (5)	1.226	C10A–O10A	1.243(5)	1.244
C10–N1	1.357 (6)	1.391	C10A–N1A	1.345(5)	1.393
N1–N2	1.390 (5)	1.393	N1A–N2A	1.385(5)	1.394
N2–C3	1.362 (6)	1.404	N2A–C3A	1.349(6)	1.408
C3–S5	1.673 (5)	1.661	C3A–S5A	1.702(4)	1.659
C3–N4	1.331 (6)	1.404	C3A–N4A/ C3A–N4B	1.350(11)/ 1.331 (10)	1.406

However, in corrosive chloride-containing environments, localized corrosion occurs on surface of zinc and its alloys, producing cavities and grooves beneath the corrosion product layer, which could accelerate the corrosion of zinc substrates [2,3].

The utilization of organic and inorganic compounds as inhibitors has proven highly effective, as they either adsorb onto surface or chemically interact with metal to form a protective barrier against corrosive environments [7–10]. Organic compounds containing potential donor atom (s) such as P, N, O, or S, along with multiple bonds in their structures, typically act as efficient corrosion inhibitors [11,12]. Theoretical studies provided molecular-level insights into inhibitor-metal interactions at the interface, thereby offering crucial information for understanding inhibition mechanisms [13,14]. It is generally believed that the mechanism involves the donation of lone pairs from heteroatoms and π-electrons from multiple bonds to the vacant *d*-orbitals of corroded metals, resulting in the formation of surface metal-inhibitor complexes. Subsequently, the substrate surface becomes covered and shielded from corrosive media [13,15].

Thiosemicarbazide and its derivatives, containing potential donor atoms such as hard O, soft S, and borderline N, could effectively inhibit metal corrosion in aggressive media [16–20]. Recently, the inhibitory behavior of several thiosemicarbazide derivatives against steel alloy corrosion in acidic environments has been examined [16–18]. These

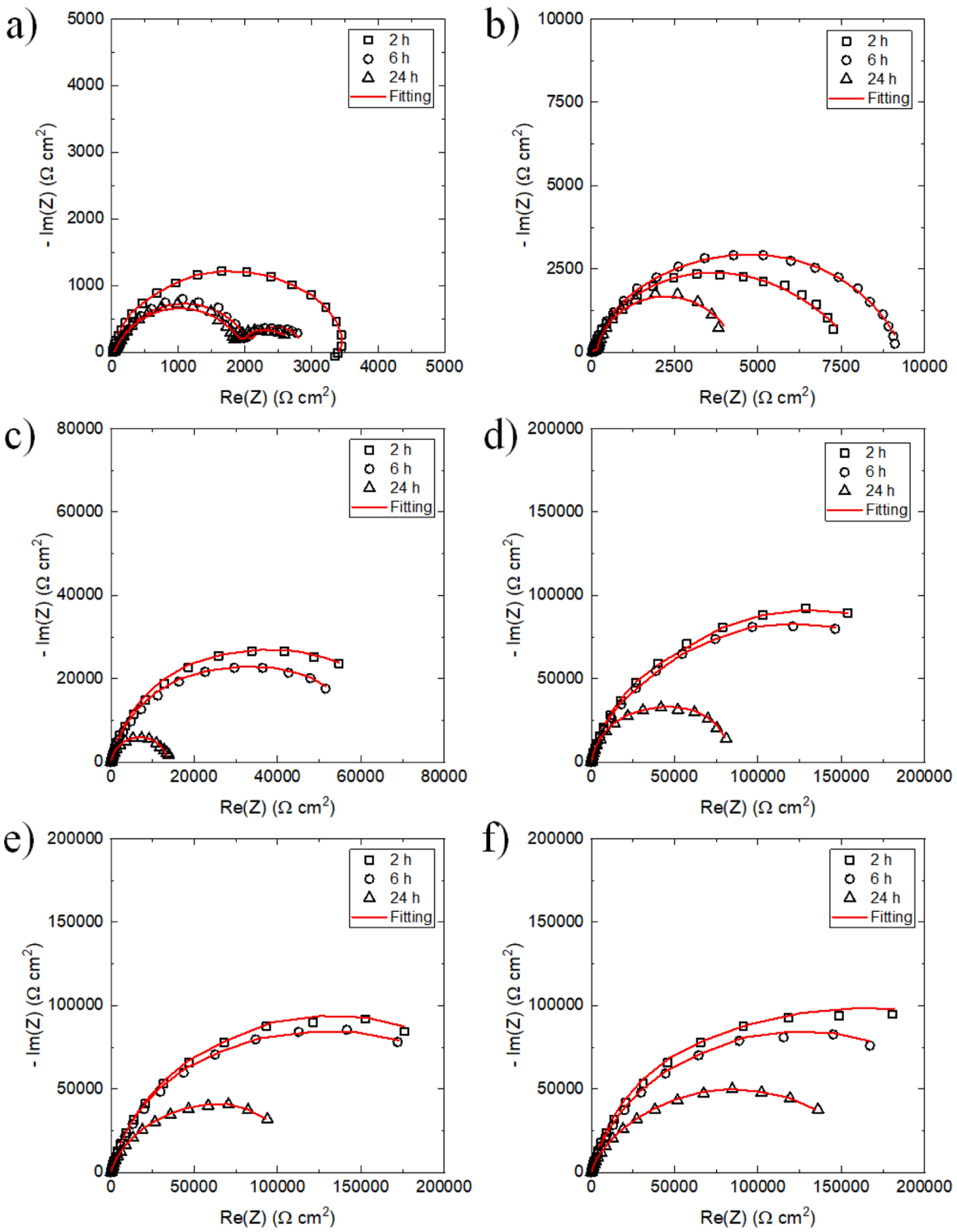

Fig. 3. Nyquist plots for the corrosion of zinc in 0.1 M NaCl solution without inhibitor (a), and with 1.0×10^{-5} M **HL**^{1} (b), 1.0×10^{-4} M **HL**^{1} (c), 1.0×10^{-3} M **HL**^{1} (d), 1.0×10^{-3} M **HL**^{2} (e), 1.0×10^{-3} M **HL**^{3} (f).

studies demonstrated that these compounds behaved as mixed-type inhibitors, with their effectiveness in enhancing substrate corrosion resistance increasing at higher concentrations [16–18]. Furthermore, thiosemicarbazide derivatives have been shown to significantly improve corrosion resistance in aluminum, magnesium, and copper alloys under various experimental conditions [19–21]. It is believed that this considerable improvement is attributed to the adsorption of these compounds onto the metal surface through interactions involving heteroatoms [16,19]. However, despite their proven effectiveness on various metal substrates, the corrosion inhibition performance of thiosemicarbazide derivatives on zinc alloys and galvanized steel remains largely unexplored, and has been studied primarily in acidic media. The behavior of thiosemicarbazide derivatives on zinc-based substrates in neutral saline environments, which are critical for many practical applications, has not been systematically investigated. In this context, the present work provides a comprehensive evaluation of three acyl

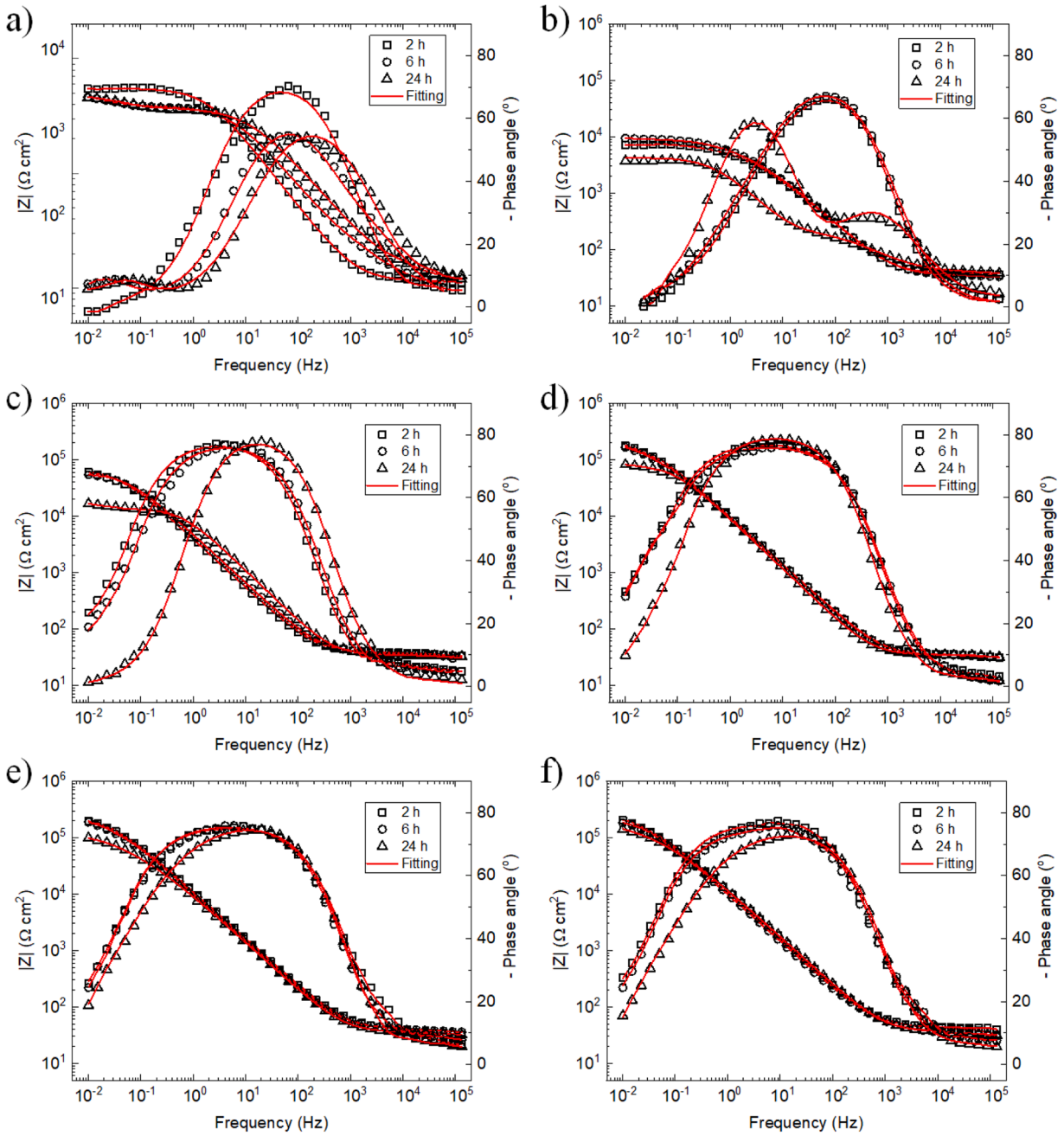

Fig. 4. Bode plots for the corrosion of zinc in 0.1 M NaCl solution without inhibitor (a), and with 1.0×10^{-5} M **HL**^{1} (b), 1.0×10^{-4} M **HL**^{1} (c), 1.0×10^{-3} M **HL**^{1} (d), 1.0×10^{-3} M **HL**^{2} (e), 1.0×10^{-3} M **HL**^{3} (f).

thiosemicarbazides derived from pyridine, phenol, and aniline building blocks (Scheme 1) as corrosion inhibitors for zinc substrates in neutral saline solution. Both experimental and modeling approaches were employed to elucidate the complex corrosion inhibition behavior of the inhibitor candidates. Electrochemical techniques, including polarization curves and EIS, were used to assess the inhibition efficiency of the compounds. Surface characterization of zinc substrates after immersion in saline solution, with and without the compounds, was conducted using XPS and FE-SEM/EDS analyses to examine the morphology and nature of surface protective film. DFT simulations were performed to reveal cooperative contributions involved in inhibition actions, considering molecular electronic and spatial features, adsorption behavior, and underlying intermolecular interactions. Supportive theoretical studies further enabled a deeper understanding of the structure-performance correlations within the studied acyl thiosemicarbazides and may provide guidance for the future design of novel inhibitors against metal corrosion.

2. Materials and methods

2.1. Materials

Industrial zinc (Vietchem, Vietnam) with following chemical composition: Zn (96.16%), C (2.41%), and O (1.43%) was used for this study. Zinc plates with a surface area of 1 cm^2 were sealed with resin. Prior to the corrosion tests, all samples were abraded sequentially with 100, 400, 800, and 1200 grit SiC papers, then rinsed with water, and ethanol (EtOH), and finally dried.

Table 2
The circuit fitted parameters.

Medium	Exposure time (h)	CPE_f (Ω^{-1} s^n cm^{-2})	n_f	R_f (Ω cm^2)	CPE_{dl} (Ω^{-1} s^n cm^{-2})	n	R_{ct} (Ω cm^2)	$\|Z\|_{10mHz}$ (Ω cm^2)	IE (%)
0.1 M NaCl	2	-	-	-	2.96×10^{-5}	0.85	3594	3452	-
	6	1.96×10^{-5}	0.75	2129	6.24×10^{-3}	0.80	708	2077	-
	24	2.13×10^{-5}	0.75	1971	6.19×10^{-3}	0.80	615	2067	-
0.1 M NaCl + 1.0×10^{-5} M **HL^1**	2	-	-	-	2.79×10^{-5}	0.80	8072	7164	-
	6	-	-	-	2.26×10^{-5}	0.81	9315	9050	-
	24	4.52×10^{-5}	0.7	260	6.41×10^{-5}	0.90	4571	3887	46.47
0.1 M NaCl + 1.0×10^{-4} M **HL^1**	2	-	-	-	2.72×10^{-5}	0.88	63620	59613	-
	6	-	-	-	2.97×10^{-5}	0.90	56880	54420	-
	24	-	-	-	3.30×10^{-5}	0.89	17670	16600	85.36
0.1 M NaCl + 1.0×10^{-3} M **HL^1**	2	-	-	-	2.03×10^{-5}	0.86	296800	177987	-
	6	-	-	-	2.23×10^{-5}	0.86	271300	166674	-
	24	-	-	-	2.43×10^{-5}	0.87	93200	82128	97.22
0.1 M NaCl + 1.0×10^{-3} M **HL^2**	2	-	-	-	1.79×10^{-5}	0.85	339400	195098	-
	6	-	-	-	1.83×10^{-5}	0.85	325100	188853	-
	24	-	-	-	2.19×10^{-5}	0.85	118600	99097	97.82
0.1 M NaCl + 1.0×10^{-3} M **HL^3**	2	-	-	-	9.84×10^{-6}	0.87	423200	203884	-
	6	-	-	-	1.74×10^{-5}	0.87	321100	183557	-
	24	-	-	-	2.06×10^{-5}	0.86	183700	141132	98.59

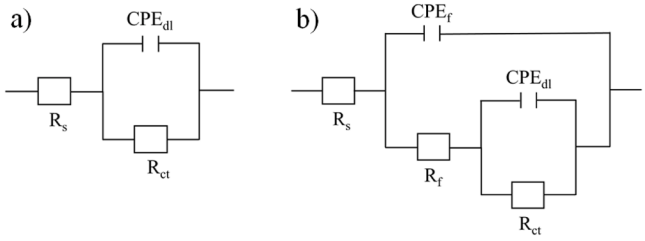

Fig. 5. EECs for fitting the EIS data.

2.2. Spectroscopic characterization

Melting points were measured in open capillary tubes using a STUART SMP3 apparatus (Bibby Sterilin, UK). IR spectra were recorded on a Shimadzu IRAffinity-1S spectrometer in the range 400- 4000 cm^{-1}. NMR spectra in DMSO-d_6 were obtained on a Bruker Avance III^{TM} HD 500 MHz multinuclear spectrometer. ESI mass spectra were taken with either an LTQ Orbitrap XL (Thermo Scientific) or an X500 QTOF (SCIEX) instrument. All MS results were reported as m/z assignments. Elemental analysis for C, H, N, and S was performed on a Heraeus vario EL elemental analyzer. The spectroscopic data, including IR, NMR, and MS spectra, and corresponding signal assignments (Table S1 and S2) are provided in the Supplementary Information.

2.3. Preparation of acyl thiosemicarbazides

Picolinoyl N4-phenylthiosemicarbazide (**HL^1**) was synthesized according to a standard method [22,23]. The acyl thiosemicarbazides containing phenol and aniline moieties were prepared following a similar procedure. Under a nitrogen atmosphere, phenyl isothiocyanate (1.2 mL, 0.01 mol) was added dropwise to a solution of the corresponding carboxylic acid hydrazides, namely 2-hydroxybenzohydrazide (1.52 g, 0.01 mol) or 2-aminobenzohydrazide (1.51 g, 0.01 mol), in absolute EtOH (30 mL). The reaction mixtures were refluxed for 1 h and then cooled down to room temperature. During these processes, the pure products were deposited as colorless solids, which were washed several times with EtOH, and finally dried in vacuo.

Salicyloyl N4-phenylthiosemicarbazide (**HL^2**): Colorless solid. Melting point: 156.5°C. Yield: ~64% (3.67 g). Elemental analysis: Calcd. for $C_{14}H_{13}O_2N_3S$: C, 58.52; H, 4.56; N, 14.62; S, 11.16%. Found: C, 58.72; H, 4.64; N, 14.26; S, 10.97%. IR (KBr, cm^{-1}): 3197(s, ν(OH)) + ν(NH)), 3063(m), 2964(w), 1657(s, ν(C=O)), 1641(s), 1606(s, ν(C=C)$_{ar}$), 1534(s, Thioamide I), 1476(s), 1450(m, Thioamide II), 1351 (w), 1310(w), 1269(w), 1233 (m, Thioamide III), 1210(m), 1148(m),

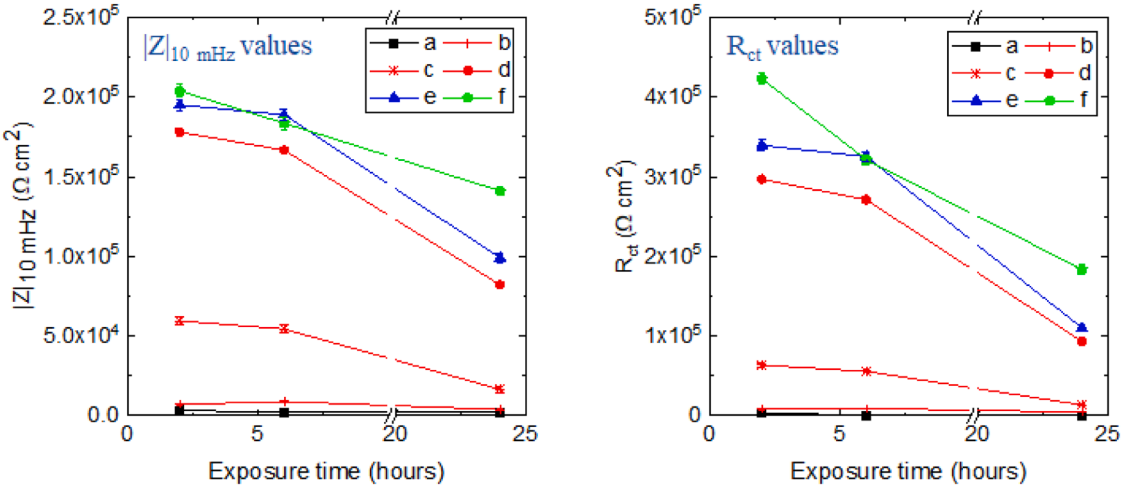

Fig. 6. The $|Z|_{10\ mHz}$ and R_{ct} values of zinc in 0.1 M NaCl solution without inhibitor (a), and with 1.0×10^{-5} M **HL^1** (b), 1.0×10^{-4} M **HL^1** (c), 1.0×10^{-3} M **HL^1** (d), 1.0×10^{-3} M **HL^2** (e), 1.0×10^{-3} M **HL^3** (f).

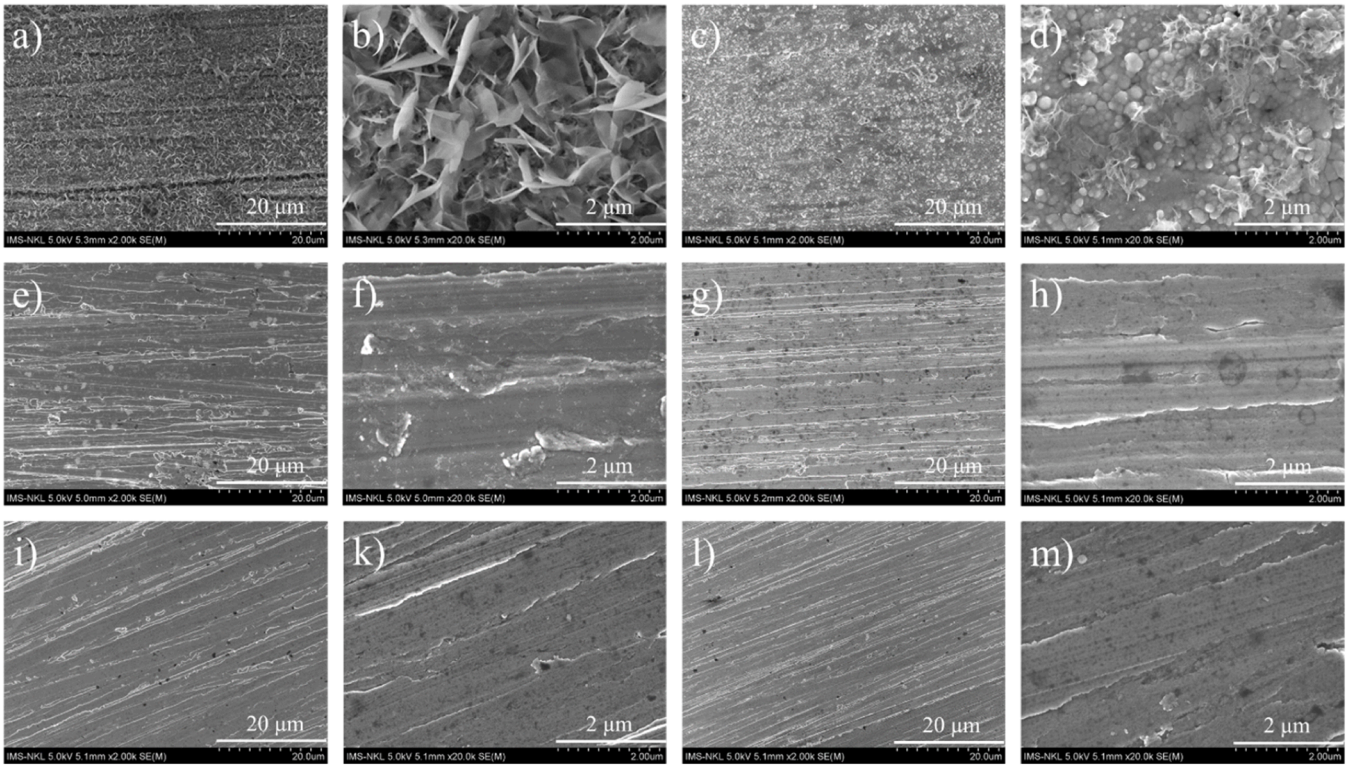

Fig. 7. Surface morphology of zinc after 24 h immersion in 0.1 M NaCl solution without inhibitor (a, b), and with 1.0×10^{-5} M **HL^1** (c, d), 1.0×10^{-4} M **HL^1** (e, f), 1.0×10^{-3} M **HL^1** (g, h), 1.0×10^{-3} M **HL^2** (i, k), 1.0×10^{-3} M **HL^3** (l, m).

Table 3
EDS analysis of the element composition on the zinc surface after 24 h exposure to 0.1 M NaCl solution in the absence and presence of **HL** inhibitors.

Medium	Element content (wt%)				
	Zn	C	N	O	S
0.1 M NaCl	81.83	2.81	-	15.36	-
0.1 M NaCl + 1.0×10^{-5} M **HL^1**	82.17	4.99	0.43	12.24	0.17
0.1 M NaCl + 1.0×10^{-4} M **HL^1**	89.12	6.04	0.69	3.83	0.32
0.1 M NaCl + 1.0×10^{-3} M **HL^1**	89.83	6.42	0.86	2.45	0.44
0.1 M NaCl + 1.0×10^{-3} M **HL^2**	90.06	6.09	0.84	2.60	0.41
0.1 M NaCl + 1.0×10^{-3} M **HL^3**	89.89	6.18	0.87	2.66	0.40

1100(w), 1033(w), 933(w), 900(m), 827(w), 773(w), 749(s, ν(C=S)), 692(s), 641(m), 566(w), 481(w). ^{1}H NMR (DMSO-d$_6$, ppm): 11.88 (s, br, 1H, N^{4}H); 9.87 (s, br, 2H, N^{1}H, OH); 7.89 (s, 1H, phenol); 7.48 (s, br, 1H, phenol); 7.42 (t, J = 7.5 Hz, 2H, phenyl); 7.34 (t, J = 7.5 Hz, 2H, phenyl); 7.16 (t, J = 7.5 Hz, 1H, phenyl); 6.96 (d, J = 7.5 Hz, 1H, phenol); 6.93 (t, J = 7.5 Hz, 1H, phenol). ^{13}C{^{1}H} NMR (DMSO-d$_6$, ppm): 181.0 (C=S); 169.0 (C=O); 159.6 (phenol); 139.2 (phenyl); 134.1, 128.9 (phenyl), 128.2 (phenol), 125.9 (phenol), 125.1 (phenyl); 119.0, 117.2, 115.3 (phenol). ESI$^+$ MS (m/z): 310.0601 (calcd. 310.0621), 100% [**HL^2** + Na]$^+$. Single crystals suitable for X-ray structure determination were acquired by slowly evaporating filtrate at ambient temperature.

Anthraniloyl N4-phenylthiosemicarbazide (**HL^3**): Invory solid. Melting point: 187.7°C. Yield: ~62% (3.55 g). Elemental analysis: Calcd. for $C_{14}H_{14}ON_4S$: C, 58.72; H, 4.93; N, 19.57; S, 11.20%. Found: C, 58.92; H, 5.14; N, 19.36; S, 11.07%. IR (KBr, cm^{-1}): 3318(m, ν(NH$_2$)), 3273(m, ν(NH)), 3160 (m, ν(NH)), 3058(w), 2971(w), 1668(s, ν(C=O)), 1617(s, δ(NH$_2$)), 1594(m, ν(C=C)$_{ar}$), 1536(s, Thioamide I), 1509(s), 1488(s), 1449(m, Thioamide II), 1368(m), 1334(m), 1310(m), 1267(m, Thioamide III), 1221(m), 1181(m), 1104(w), 1029(w), 963(m), 903(w), 771(m, ν(C=S)), 744(m), 718(w), 692(m), 646(w), 615(w), 577(w), 500 (w). ^{1}H NMR (DMSO-d$_6$, ppm): 9.75 (s, 1H, N^{4}H); 9.56 (s, 1H, N^{1}H); 7.70 (d, J = 7.5 Hz, 1H, aniline); 7.50-7.42 (m, 2H, phenyl); 7.32 (t, J = 7.5 Hz, 2H, phenyl); 7.19 (t, J = 7.5 Hz, 1H, aniline); 7.15 (t, J = 7.5 Hz, 1H, phenyl); 6.73 (d, J = 7.5 Hz, 1H, aniline); 6.52 (t, J = 7.5 Hz, 1H, aniline). ^{13}C{^{1}H} NMR (DMSO-d$_6$, ppm): 181.6 (C=S); 168.8 (C=O); 150.4 (aniline); 139.4 (phenyl); 132.8 (aniline); 129.2, 128.6, 128.2, 126.2, 125.3 (phenyl), 122.6, 116.6, 114.7, 112.1 (aniline). ESI$^-$ MS (m/z): 285.0805 (calcd. 285.0815), 100% [**HL^3** – H]$^-$.

2.4. X-ray crystallography

Intensity data for the diffraction of **HL^2** were collected at 293 K on a Bruker D8 Quest diffractometer using a TRIUMPH monochromator with Mo Kα radiation (λ = 0.71073 Å). The APEX3 software was exploited for data reduction [24], while the data was corrected for absorption using the SADABS program [25]. Structure was solved and refined by the SHELXT and SHELXL 2014/7 programs [26,27]. The molecular structures were represented using the program OLEX2–1.5 [28]. Summary of crystallographic data and structure calculations is presented in Table S3.

2.5. Surface characterization

The top morphology of zinc substrates after immersion in saline solution with and without inhibitors was studied via FE-SEM (S4800, Hitachi). Elemental compositions of the surface samples were detected by EDS at an accelerating voltage of 20 kV.

The surface products formed on zinc substrate after immersion in saline solution containing acyl thiosemicarbazides (**HL**) were analyzed by XPS (PHI VERSAPROBE 5000) using Al Kα radiation (1486.6 eV). Measurements were performed with an X-ray source operating at 50 W and a beam diameter of 200 µm. Atomic compositions were calculated from peak areas applying a Shirley baseline correction.

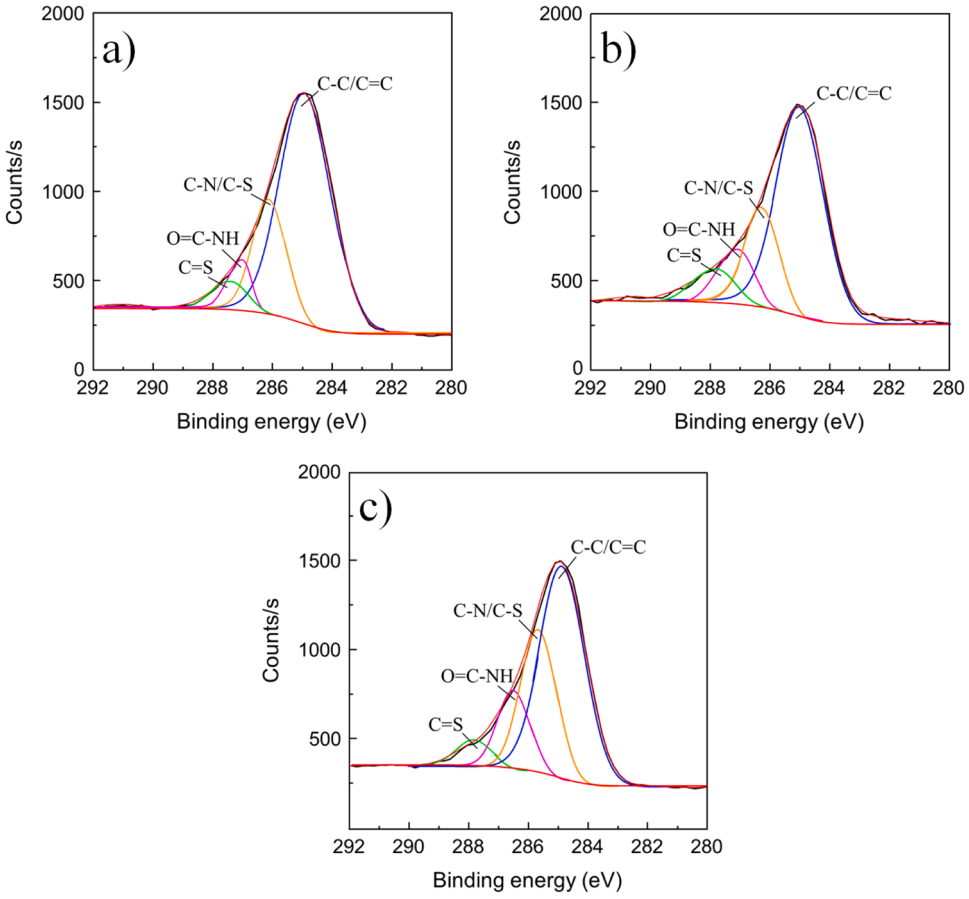

Fig. 8. High-resolution XPS spectra of C 1 s for the zinc substrate surface after 24 h exposure to 0.1 M NaCl solution with 1.0×10^{-3} M **HL**^{1} (a), 1.0×10^{-3} M **HL**^{2} (b), and 1.0×10^{-3} M **HL**^{3} (c).

2.6. Electrochemical tests

The corrosion protection of zinc substrate in saline solution, with and without inhibitors, was investigated via EIS and polarization curves by using a VSP 300 Biologic. A three-electrode system was employed, consisting of an Ag/AgCl (saturated KCl) reference electrode, a platinum mesh counter electrode, and a working electrode with an exposed surface area of 1 cm^2. The EIS test was performed between 100 kHz and 10 mHz with an amplitude perturbation of 10 mV. Polarization curves were obtained with potential range from 0.03 V to –0.30 V and –0.03 to +0.30 V versus open circuit potential (V vs. Ag/AgCl) at a scan rate of 0.2 mV s^{-1}. Electrochemical tests of all samples were repeated three times. Impedance spectra were analyzed using the commercial software ZSimpWin, and the inhibition efficiency (IE) after 24 h of immersion was calculated using the following equation [29]:

$$IE(\%) = \left(R_{all}^{inh} - R_{all}^{0}\right)/R_{all}^{inh} \times 100\%$$

where R_{all}^{0} and R_{all}^{inh} $\left(R_{all} = R_f + R_{ct}\right)$ represent the overall corrosion impedance of zinc substrates in blank saline solution and inhibitor-containing solutions, respectively.

2.7. Theoretical calculations

The structure of **HL**^{2} in the gas phase was optimized using DFT at the PBE-D3(BJ)/def2-TZVP level of theory [30–33] implemented in the ORCA 5.0 package [34]. Both *syn* and *anti* conformations arising from the relative orientation of the –OH and –C=O groups were considered. Frequency calculations were performed to confirm the nature of the optimized structures. Molecular electrostatic potential (MEP) surface were computed both at a finite DFT level using the Gaussian 16 package [35], and at a periodic DFT level using the Vienna *Ab initio* Simulation Package (VASP) [36,37]. Fukui indices were evaluated at the B3LYP/def2-TZVP level of theory [30–33] using Gaussian 16 [35]. **HL**^{1}, **HL**^{2}, and **HL**^{3} molecules were first fully optimized in their neutral states, followed by single-point calculations of the corresponding anionic and cationic species without geometry reoptimization. The electrophilic ($f^{(-)}$), nucleophilic ($f^{(+)}$) and radical ($f^{(0)}$) Fukui indices were determined from the resulting charge differences using the UCA-Fukui (v2.1) code [38]. The interaction between the three acyl thiosemicarbazides (**HL**^{1}, **HL**^{2}, and **HL**^{3}) and the zinc surface was further investigated at a quantum-chemical level. All calculations were performed at a periodic DFT level using the VASP [36,37]. The projected augmented wave (PAW) scheme was applied with a plane wave cutoff of 500 eV. The PBE functional was employed for exchange-correlation with van der Waals interactions described using the Grimme correction (DFT-D3 method) [33]. Since the experimental XPS spectra pointed to oxidation of the zinc surface after 24 h exposure (Zn-O, Zn-OH signatures), both pristine Zn and zinc oxide surfaces were considered in the calculations. The (0001) Zn surface and (10-10) ZnO surface, i.e., the stoichiometric non-polar facet of ZnO with a thickness of four layers were built. A similar orthogonal Zn (ZnO) unit cell of lattice parameters $a = 13.11$ (12.95) Å, $b = 13.62$ (10.44) Å, and $c = 35.00$ Å was used for the three systems. The inhibitor molecule and the first top Zn (ZnO) layer were allowed to relax prior to interface property calculations. Atomic charges and bond orders were computed using the DDEC6 scheme [39,40].

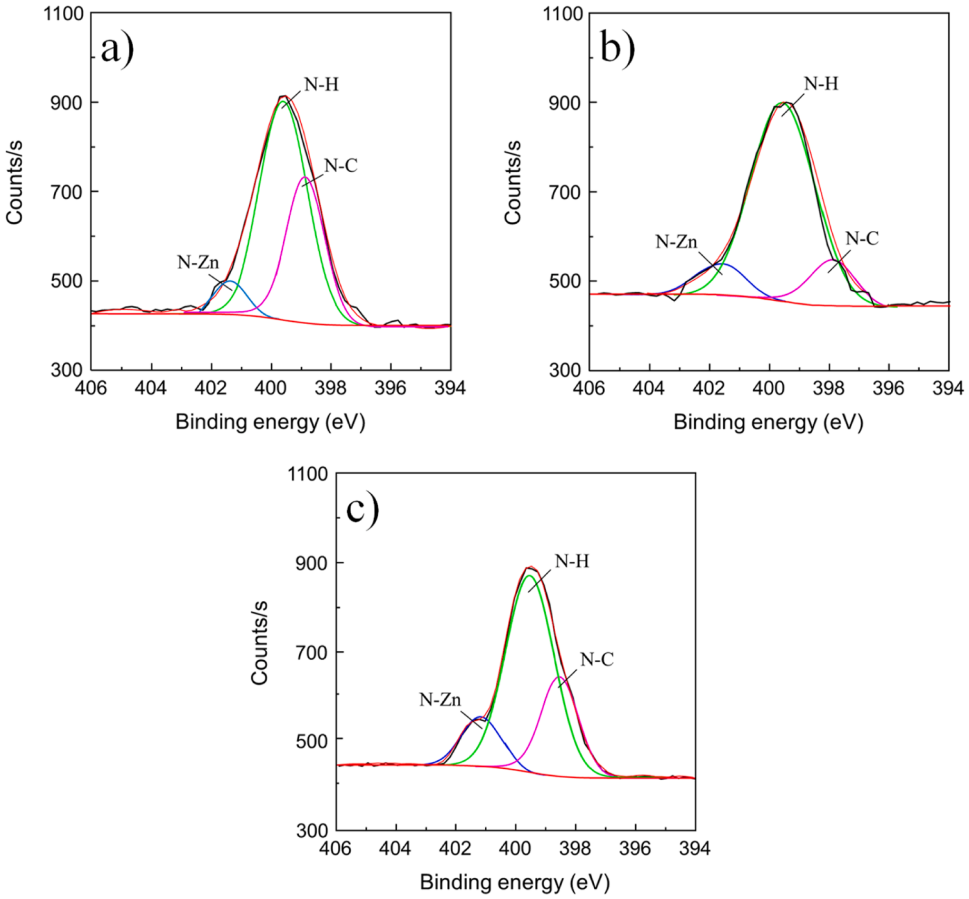

Fig. 9. High-resolution XPS spectra of N 1 s for the zinc substrate surface after 24 h exposure to 0.1 M NaCl solution with 1.0×10^{-3} M **HL**^{1} (a), 1.0×10^{-3} M **HL**^{2} (b), and 1.0×10^{-3} M **HL**^{3} (c).

3. Results and discussion

3.1. Syntheses and structural characterization of acyl thiosemicarbazides

The synthesis and characterization of picolinoyl N4-phenylthiosemicarbazide (**HL**^{1}) have been recently reported [23]. The two compounds, salicyloyl N4-phenylthiosemicarbazide (**HL**^{2}) and anthraniloyl N4-phenylthiosemicarbazide (**HL**^{3}), were obtained in fair yields by reflux of equimolar amounts of phenyl isothiocyanate with the corresponding carboxylic acid hydrazides in absolute ethanol (Scheme 2).

The expected chemical compositions of **HL**^{2} and **HL**^{3} were indicated by elemental analysis and by the presence of the fragments $[\mathbf{HL}^{2} + \mathrm{Na}]^{+}$ and $[\mathbf{HL}^{3} - \mathrm{H}]^{-}$, respectively, in the corresponding mass spectra (Fig. S4, S8). The IR spectra of both compounds (Fig. S1, S5) exhibited intense absorption bands around 1650 cm^{-1} ascribed to $\nu_{C=O}$ stretches. The C=S stretching vibration was detected by bands in the 710-760 cm^{-1} region [41], whereas three additional characteristic bands of the thioamide group (HN–C=S), namely thioamide I, thioamide II and thioamide III [41–44], were also observed in the spectra of **HL**^{2} and **HL**^{3}. Specifically, absorptions around 1534, 1450 and 1233 cm^{-1} in the case of **HL**^{2} were assigned to thioamide I, II and III, respectively, while in **HL**^{3} the corresponding bands appeared surrounding 1536, 1449 and 1267 cm^{-1} [44,45]. The appearance of distinctive bands for C=O and C=S groups together with the missing of absorptions above 3500 cm^{-1} and near 2600 cm^{-1} revealed the ketone-thioketone tautomers of the compounds in the solid state. The NH groups were identified not only by broad absorptions in the range 3300-3100 cm^{-1} within the IR spectra, but also by the most downfield broad singlets in the proton NMR spectra (Fig. S2, S6) [22,46]. The remaining signals correspond to protons in the phenyl and phenylene rings, consistent with resonances in the typical aromatic region. In the $^{13}C\{^{1}H\}$ NMR spectra, signals for aromatic carbons were found between 110-150 ppm, while the downfield signals around 180 and 160 ppm were assigned to the C=S and C=O groups, respectively [47–49]. Thus, the expected compositions and structures of the acyl thiosemicarbazides were strongly confirmed by the supportive spectroscopic data. In the case of **HL**^{2}, such results were ascertained by X-ray structure determination. The compound crystallized in the triclinic space group $P\bar{1}$ with two crystallographically independent molecules in the asymmetric unit. These molecules interacted via intermolecular hydrogen bond between the amide N4H group and the carbonyl O10 atom (Fig. 1). Selected bond lengths are listed in Table 1.

Both molecules in the asymmetric unit adopted twisted conformations. In particular, the dihedral angles between mean planes of the salicyolyl and thiosemicarbazide moieties in the molecule labeled with suffix A and in the second molecule were 79.77(6)° and 88.14(4)°, respectively. Similar conformational features were found in structures of acyl 4-phenylthiosemicarbazides recently reported [23,50,51]. The pronounced double-bond character of C–$O_{carbonyl}$ and C–S bonds strongly confirmed the ketone-thioketone tautomeric form of **HL**^{2} in the solid state, which could be pointed out from the IR spectroscopic results. Additionally, the delocalization of π-electron within the carbonyl-thiosemicarbazide skeleton was evidenced by the partial π-bond character in the N–N and C–N bonds (Table 1). It is noteworthy that, in the asymmetric unit, two independent molecules exhibit distinct conformations determined by the relative orientation of the –OH and –C=O groups. The molecule labeled with suffix A adopts *syn* configuration, while the other displays the *anti* conformation. Similar conformations have been reported for acyl thiosemicarbazides [23,51]. The presence of two conformational isomers in the crystal structure could

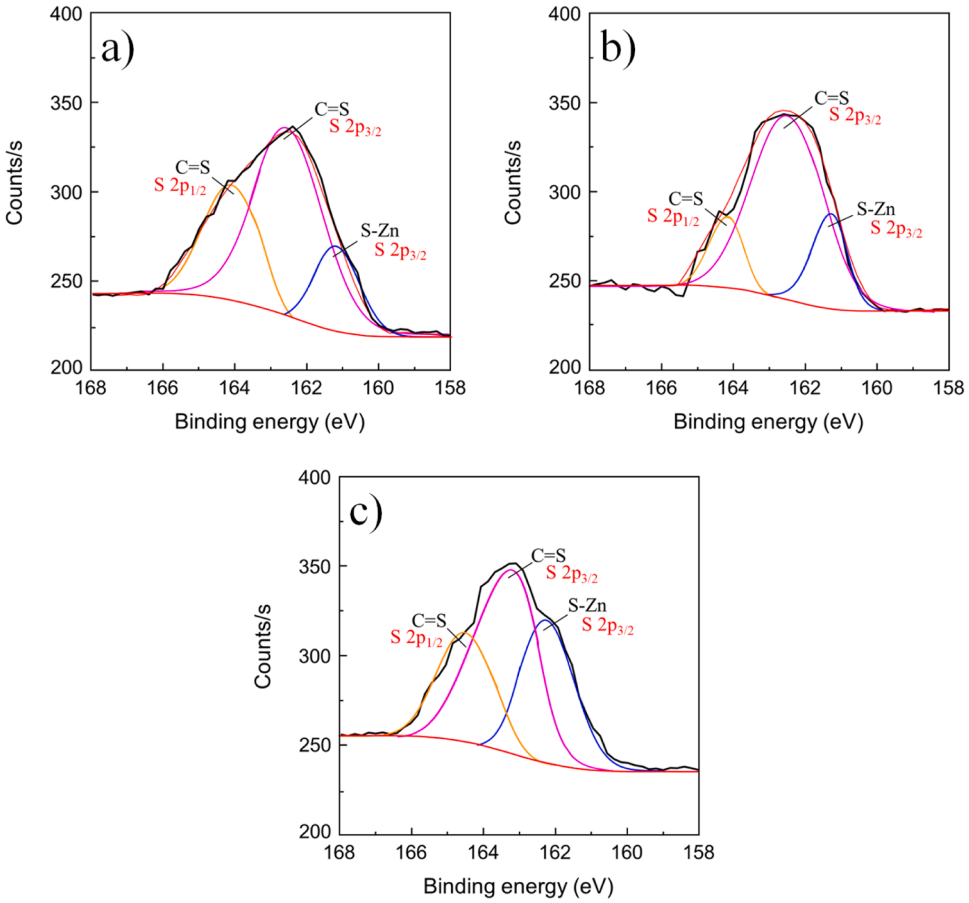

Fig. 10. High-resolution XPS spectra of S 2p for the zinc substrate surface after 24 h exposure to 0.1 M NaCl solution with 1.0×10^{-3} M **HL**^{1} (a), 1.0×10^{-3} M **HL**^{2} (b), and 1.0×10^{-3} M **HL**^{3} (c).

result from a slight difference in the relative stability of the two forms. In order to obtain convincing evidence for this stability difference, the isomerization free energy between the *syn* and *anti* forms of **HL**^{2} was calculated using DFT. The optimized structures showed good agreement with the X-ray crystallographic data (Table 1 and Fig. S9). The isomerization free energy at 298 K is approximately 25 kJ mol^{-1}, favoring the *syn* isomer. This energy difference could be compensated by crystal-packing forces [52].

3.2. Corrosion inhibition of thiosemicarbazide derivatives on zinc in saline solution

In this research, the corrosion behavior of zinc in a neutral chloride environment was examined, as such conditions promote localized corrosion. While the Tafel method is limited to determining the average uniform corrosion rate, it cannot be employed to assess localized corrosion [10,53]. Moreover, using a low scan rate (0.2 mV s^{-1}) may introduce current bias, leading to inaccurate current density estimates [10]. Thus, polarization curves were utilized to qualitatively assess the corrosion behavior of zinc in 0.1 M NaCl solution in the absence and presence of **HL** compounds.

To evaluate the concentration effect of **HL**^{1}, polarization curves were recorded after 24 h immersion in NaCl solution containing varying **HL**^{1} concentrations (0 - 1.0×10^{-3} M) (Fig. 2). Relative to inhibitor-free solution, the curves showed a marked decrease in both anodic and cathodic current densities, suggesting that **HL**^{1} suppressed both anodic zinc dissolution and the cathodic reduction process [54,55]. A further continuous decrease in current density with increasing **HL**^{1} concentration demonstrated improved inhibition efficiency at higher concentrations within the studied range. On the anodic curve, the emergence of a plateau with increasing **HL**^{1} concentration suggested that adsorption of more **HL**^{1} molecules produced a denser barrier at zinc interface, thereby retarding anodic dissolution [56,57]. Moreover, observation of a slight positive shift in the corrosion potential confirmed that **HL**^{1} can act as a mixed-type inhibitor with predominant influence on the anodic dissolution of zinc.

The inhibiting impact of **HL**^{1} concentration on the corrosion behavior of zinc in saline solution was further studied by EIS (Fig. 3 and 4). The Nyquist plots of samples immersed in **HL**^{1} solutions presented larger capacitive arc radii compared to the sample in inhibitor-free solution, with a significant rise in arc radius as **HL**^{1} concentration increased (Fig. 3). The marked increase in |Z| values at lower frequencies in the presence of **HL**^{1} (1.0×10^{-5} - 1.0×10^{-3} M) was clear evidence that the organic compound enhanced corrosion resistance of zinc in saline solution. Interestingly, at higher **HL**^{1} concentrations, the semicircle diameter expanded markedly, and the Bode phase diagram (Fig. 4) revealed higher absolute values of the phase angle. This observation may be associated with the adsorption of **HL**^{1} molecules on the zinc surface, thereby restricting metal dissolution [58]. Additionally, at higher **HL**^{1} concentrations, the corrosion protection of the substrate became more effective. In detail, the $|Z|_{10mHz}$ values of the samples exposed to electrolyte solution containing 1.0×10^{-3} M **HL**^{1} increased by approximately 50-fold and 35-fold after 2 h and 24 h of immersion, respectively (Table 2).

To further clarify the corrosion behavior of zinc in saline solution with and without **HL**^{1}, different electrochemical equivalent circuits (EECs) were used to fit the EIS results (Fig. 5). The fitted parameters are presented in Table 2. The fact that after 2 h of immersion, all samples showed only one time constant, proved the fitness of the model $R_s(CPE_{dl}R_{ct})$ (Fig. 5a), consisting of the solution resistance (R_s), the

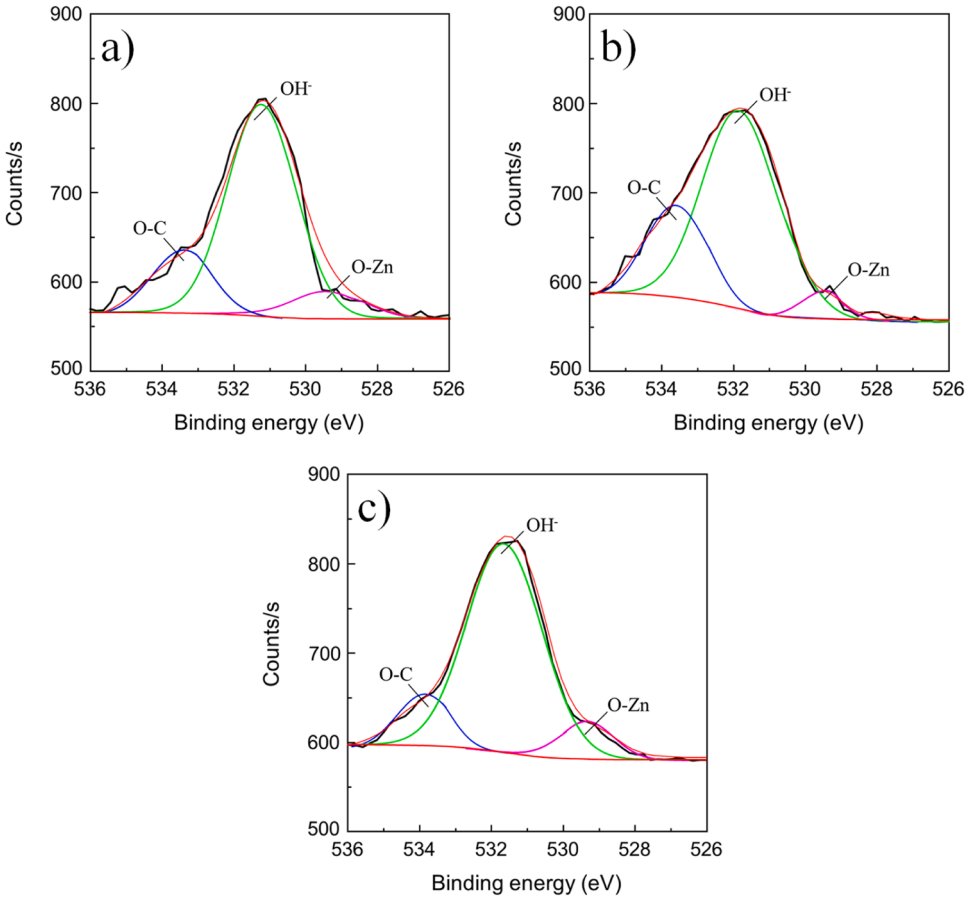

Fig. 11. High-resolution XPS spectra of O 1 s for the zinc substrate surface after 24 h exposure to 0.1 M NaCl solution with 1.0×10^{-3} M **HL**^{1} (a), 1.0×10^{-3} M **HL**^{2} (b), and 1.0×10^{-3} M **HL**^{3} (c).

charge transfer resistance (R_{ct}), and the double-layer capacitance (CPE_{dl}). The R_{ct} values in the presence of 1.0×10^{-5}, 1.0×10^{-4}, and 1.0×10^{-3} M **HL**^{1} were 8072, 63620, and 296800 Ω cm^2, respectively. Such values were much larger than those of the inhibitor-free solution, indicating that **HL**^{1} could excellently shield zinc during the initial 2 h of immersion [59]. For zinc exposed to inhibitor-free solution for 6 and 24 h, two time constants were observed, and the $R_s(CPE_f(R_f(CPE_{dl}R_{ct})))$ model was applied to fit EIS results (Fig. 5b). Here, R_s is the solution resistance, R_f and CPE_f relate to the film resistance and capacitance of the layer of corrosion products, while R_{ct} and CPE_{dl} associate with the charge transfer resistance and double-layer capacitance. The sharp decline of R_{ct} values in inhibitor-free solution to 708 and 615 Ω cm^2 after 6 and 24 h, respectively, confirmed the susceptibility of zinc to corrosion in saline solution. In contrast, zinc samples immersed in **HL**^{1}-containing solutions exhibited only one time constant after 6 h, and their R_{ct} values remained nearly constant in comparison with those after 2 h. After 24 h, two time constants at medium and low frequencies were detected in the case of solution containing 1.0×10^{-5} M **HL**^{1} (Fig. 5b), for which the $R_s(CPE_f(R_f(CPE_{dl}R_{ct})))$ model was suitable. However, after 24 h of immersion, only one time constant was observed for the samples exposed to electrolyte solutions with 1.0×10^{-4} and 1.0×10^{-3} M **HL**^{1}. Notably, after 24 h, the IE of 1.0×10^{-3} M **HL**^{1} reached 97.22%, markedly higher than at lower concentrations (85.36% for 1.0×10^{-4} M and 46.47% for 1.0×10^{-5} M). The considerable increase in R_{ct} and IE values with rising **HL**^{1} concentration and immersion time (Table 2 and Fig. 6) was probably associated with more extensive adsorption of **HL**^{1} molecules on the zinc surface, effectively blocking available active sites and isolating the substrate from the aggressive media [54].

Based on the corrosion inhibition performance of **HL**^{1} at different concentrations, the inhibitory effects of 1.0×10^{-3} M **HL**^{2} and **HL**^{3} on zinc substrate in saline solution were additionally investigated by electrochemical measurements. Similar to **HL**^{1}, the sharp decrease in current density and the slight positive shift in corrosion potential observed in the presence of 1.0×10^{-3} M **HL**^{2} and **HL**^{3} compared with the inhibitor-free solution, demonstrated that these compounds also act as mixed-type inhibitors, primarily hindering the anodic reactions (Fig. 2) [58]. At the concentration of 1.0×10^{-3} M, **HL**^{1}, **HL**^{2}, and **HL**^{3} all intensified the inhibitory effect, giving rise to more considerable reduction in anodic current density. Meanwhile, the fall of cathodic current density in the presence of all inhibitors revealed their simultaneous regulation on the kinetics of the cathodic reaction [55]. Remarkably, both cathodic and anodic current densities were lower for **HL**^{2} and **HL**^{3} than for **HL**^{1}, pointing out that **HL**^{2} and **HL**^{3} were more effective corrosion inhibitors.

The inhibition efficiency of **HL**^{2} and **HL**^{3} was also studied by EIS at different exposure times (Figs. 3 and 4). Similar to **HL**^{1}, the |Z| values at lower frequency became larger upon the addition of **HL**^{2} and **HL**^{3} (Table 2 and Fig. 6). However, during the exposure period, the phase angles of samples in electrolyte solutions containing **HL**^{2} and **HL**^{3} were higher than those found with **HL**^{1}. The considerably high $|Z|_{10mHz}$ values of samples with **HL**^{2} and **HL**^{3} were likely attributed to the greater stability of their adsorbed molecules on the zinc surface compared with **HL**^{1}. As with the saline solution with 1.0×10^{-3} M **HL**^{1}, only one time constant was found for zinc substrate in the presence of 1.0×10^{-3} M **HL**^{2} and **HL**^{3} during the exposure time, supporting the $R_s(CPE_{dl}R_{ct})$ model (Fig. 5a). It was believed that the presence of **HL**^{2} and **HL**^{3} was responsible for a substantial increase in R_{ct} and a gradual decrease in CPE_{dl} values compared with the inhibitor-free solution, confirming their effectiveness in corrosion protection (Table 2). At the same concentration and after the first 2 h, **HL**^{3} presented the highest R_{ct} values among the three inhibitors (Fig. 6). After 6 h, the R_{ct} values of **HL**^{3}-containing

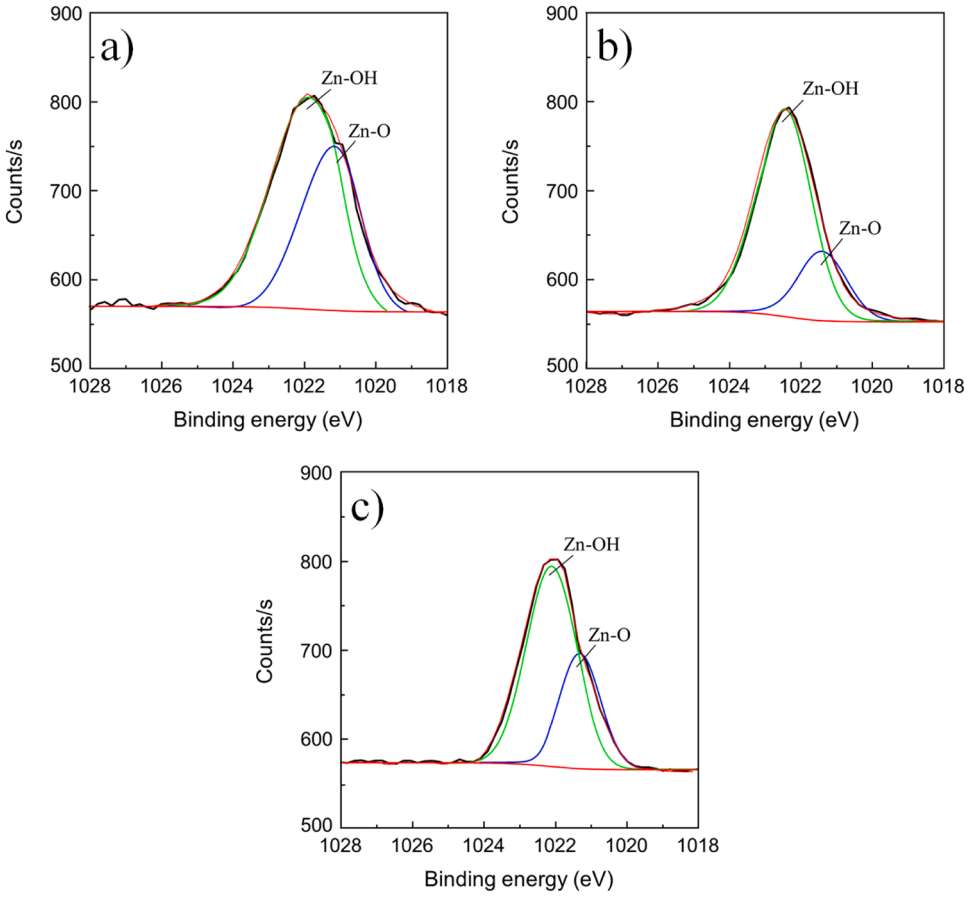

Fig. 12. High-resolution XPS spectra of Zn $2p_{3/2}$ for the zinc substrate surface after 24 h exposure to 0.1 M NaCl solution with 1.0×10^{-3} M **HL**^{1} (a), 1.0×10^{-3} M **HL**^{2} (b), and 1.0×10^{-3} M **HL**^{3} (c).

solution decreased significantly, whereas, those of **HL**^{2} exhibited only a slight decline. However, after 24 h, the R_{ct} values of all inhibitors remarkably decreased. Despite this reduction, the order of R_{ct} remained **HL**^{3} > **HL**^{2} > **HL**^{1} at the same concentration, reflecting their relative stability. At 1.0×10^{-3} M, **HL**^{2} and **HL**^{3} demonstrated superior corrosion protection, with inhibition efficiencies of 97.82% and 98.59%, respectively, compared to 97.22% for **HL**^{1}. The adsorption of **HL** molecules on the zinc surface initially prevented direct contact with the corrosive environment, thereby increasing R_{ct} values. However, chloride anions could diminish this adsorption, leading to desorption and the initiation of pitting corrosion [2,13]. Such influence would be the reason for the lower R_{ct} and $|Z|_{10mHz}$ values during prolonged exposure. Overall, the EIS results confirmed that **HL**^{1}, **HL**^{2}, and **HL**^{3} provided excellent corrosion protection for zinc substrate after 24 h, with **HL**^{3} showing the highest anti-corrosion ability at the same concentration.

3.3. Surface composition analysis

The surface morphologies of zinc substrates after 24 h exposure in 0.1 M NaCl solution without and with **HL** inhibitors were examined by FE-SEM (Fig. 7), while the surface compositions were analyzed by EDS (Table 3). After 24 h of immersion in the inhibitor-free solution, corrosion products with a micro-porous structure formed and covered the entire zinc surface (Fig. 7a and b). The elevated O wt% in the EDS spectrum confirmed the deposition of a great amount of oxygen-containing corrosion products [2]. In the presence of 1.0×10^{-5} M **HL**^{1}, crystalline spherical corrosion products were observed (Fig. 7c and d), the detection of N and S elements in EDS (Table 3) exposed the adsorption of **HL**^{1} molecules onto the zinc surface. The higher O content under this condition was further indicative of the formation of zinc oxide/hydroxide layers. By contrast, in solutions containing 1.0×10^{-4} and 1.0×10^{-3} M **HL**^{1}, there was no severe corrosive attack by the medium (Fig. 7e–h), coinciding with the appearance of only one time constant in the Bode plots. Although selective corrosion was still noticeable at these concentrations, its extent decreased with increasing **HL**^{1} concentration. The corresponding EDS data (Table 3) presented the lower O but higher N and S contents, confirming enhanced adsorption of **HL**^{1} molecules on the zinc surface, which impeded chloride attack and thus, effectively suppressed corrosion. Similarly, the zinc surfaces exposed to 1.0×10^{-3} M **HL**^{2} and **HL**^{3} also showed minimal corrosion damage (Fig. 7). In fact, the zinc substrates with **HL**^{2} and **HL**^{3} appeared slightly smoother than those with **HL**^{1}, agreeing with their higher corrosion resistance realized in the EIS results. Although organic inhibitor films formed by adsorption of **HL**^{1}, **HL**^{2}, and **HL**^{3} were not visually distinguishable, the nearly intact zinc surfaces and the content of N and S elements in EDS results validated the adsorption of inhibitor molecules and their protective function (Table 3).

XPS analysis was employed to study in more detail the chemical composition and interactions of protective films formed on zinc after 24 h of immersion in 0.1 M NaCl solution with 1.0×10^{-3} M **HL**^{1}, **HL**^{2}, and **HL**^{3}. The full-range XPS spectra of zinc surfaces in the presence of **HL** inhibitors revealed the presence of carbon, nitrogen, sulfur, oxygen, and zinc elements (Fig. S10). The detection of nitrogen and sulfur confirmed the adsorption of **HL** molecules and the formation of **HL**-containing films on the zinc surface.

The high-resolution C 1 s spectra displayed four main peaks corresponding to four different types of C atoms on zinc surface after exposure to inhibitor solutions (Fig. 8). The most intensive peak of C 1 s at about 284.7 eV was related to C–C/C=C bonds from organic compounds [60,61]. The other three peaks at about 288, 287.2, and 286.5 eV correspond

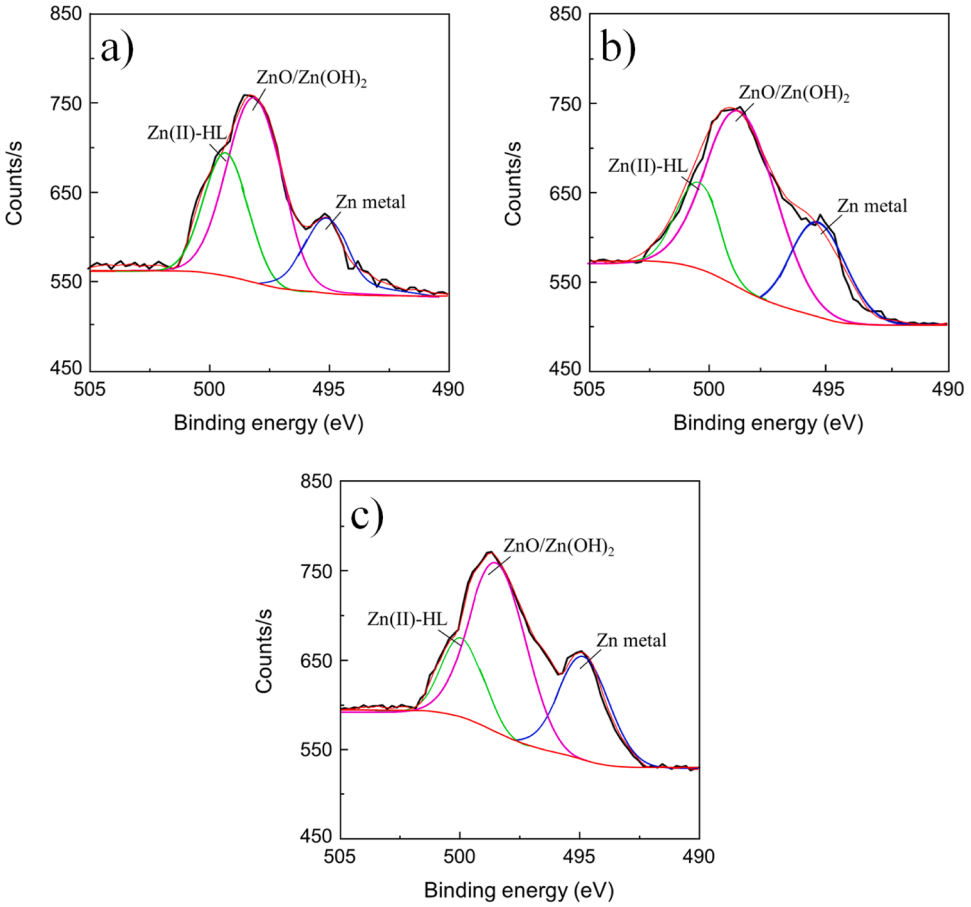

Fig. 13. High-resolution XPS spectra of Zn LMM for the zinc substrate surface after 24 h exposure to 0.1 M NaCl solution with 1.0×10^{-3} M **HL**^{1} (a), 1.0×10^{-3} M **HL**^{2} (b), and 1.0×10^{-3} M **HL**^{3} (c).

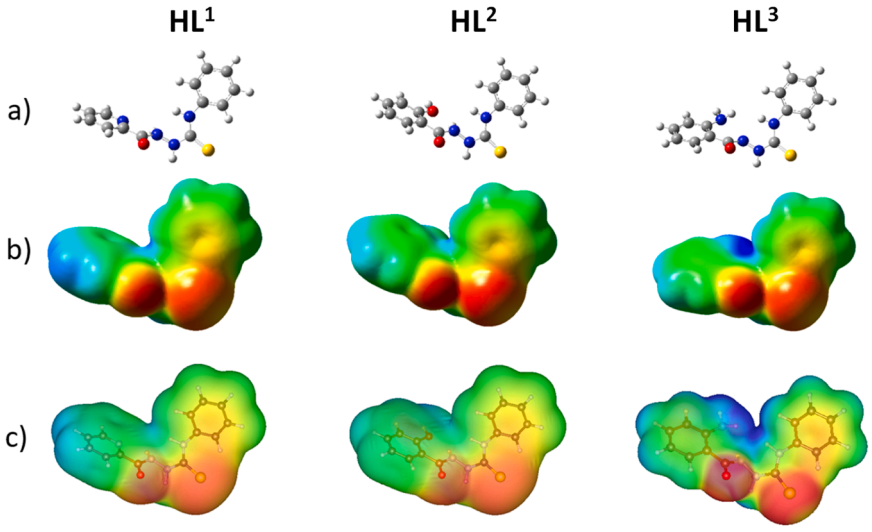

Fig. 14. MEP surfaces computed at (b) finite and (c) periodic DFT levels. Isovalues are set from $-5e^{-2}$ (red) to $+5e^{-2}$ (blue).

to C–N, C–O, and C–S of bonds of the inhibitors, respectively (Fig. 8) [60, 61]. Notably, the absence of C–metal bonds in the C 1 s spectra of all samples proved the lack of interaction between zinc ions and carbon atoms.

The N 1 s spectra of all samples exhibited two peaks around 399.8 eV and 398.2 eV, attributed to nitrogen atoms in the functional groups N–H and N–C, respectively, of the inhibitor molecules (Fig. 9) [60,61]. The peak intensity corresponding to the N–C bond in **HL**^{1} was higher than in **HL**^{2} and **HL**^{3}. It seems that this discrepancy was due to the pyridinyl ring within **HL**^{1} molecule (Scheme 1). In addition, all samples exhibited a peak at around 401.5 - 402.0 eV, which is at a higher binding energy than N–H bonds. Since higher binding energy is associated with a larger degree of oxidation, this peak could be assigned to N–metal bonds (i.e. Zn–N bonds) [62,63]. Specifically, the coordinative bond between N

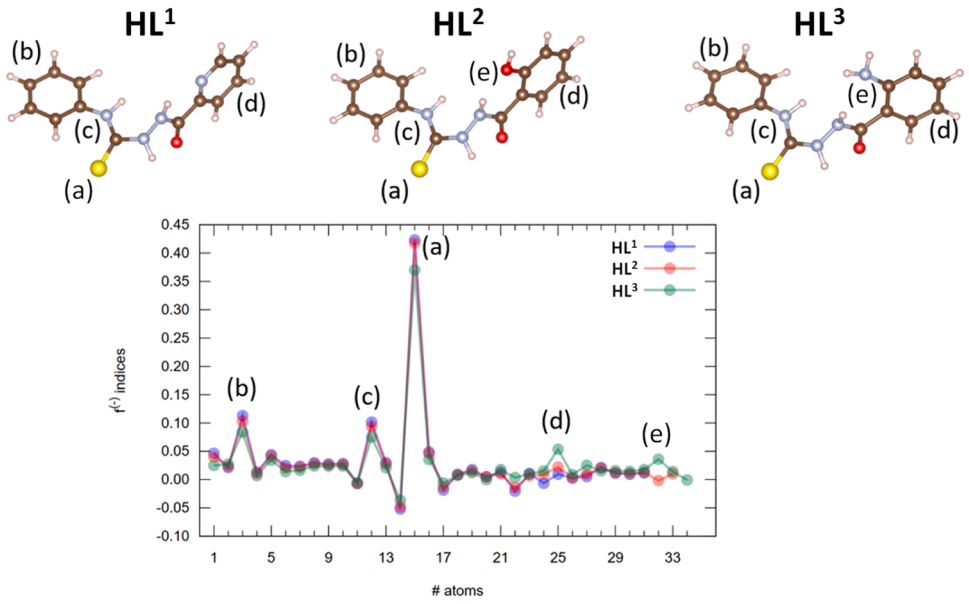

Fig. 15. Comparison of $f^{(-)}$ Fukui indices for the three compounds (**HL**^{1}-blue, **HL**^{2}-red, and **HL**^{3}-green). Atom labelling is arbitrary but was kept consistent among the three molecules for comparison. Atom #24 corresponds to the site bearing the substituent group specific to each compound: $\mathbf{N}_{\text{pyridine}}$ (**HL**^{1}), **C**–OH (**HL**^{2}) and **C**–NH_2 (**HL**^{3}).

Table 4
Computed interface properties of **HL**^{1}, **HL**^{2}, and **HL**^{3} on zinc and zinc oxide surface: adhesion energy (E_{adh}), charges on molecules (Q_{mol}), and summation of bond orders (SBO) with contributions of C, N, and S atoms.

Structure	E_{adh}	Q_{mol}	SBO			
	(eV)	(e)	Total	C	N	S
HL^1 on Zn	–2.01	+0.174	1.99	0.81	0.19	0.57
HL^1 on ZnO	–2.22	+0.185	1.40	0.50	0.28	0.29
HL^2 on Zn	–2.20	+0.184	2.13	0.91	0.10	0.57
HL^2 on ZnO	–1.94	+0.104	1.02	0.49	0.18	0.04
HL^3 on Zn	–2.24	+0.206	2.09	0.60	0.22	0.69
HL^3 on ZnO	–3.55	+0.362	2.55	1.21	0.70	0.02

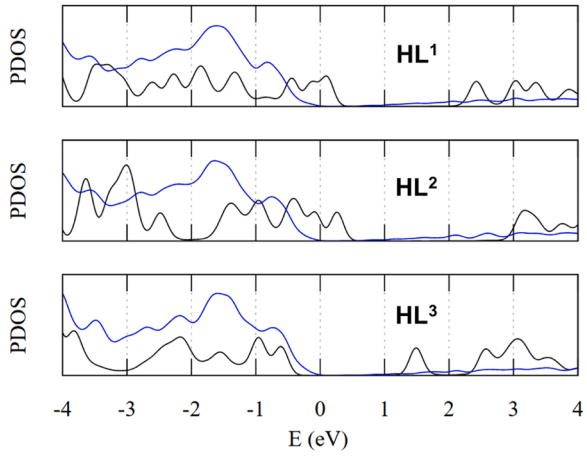

Fig. 16. PDOS of **HL**/(10-10) ZnO surface, with ZnO (blue) and **HL** (black). The top of the valence band of ZnO was used as energy reference.

donor atoms and zinc centers reduced the electron density of the N atoms and subsequently, leading to an increase in binding energy [62,63].

The S 2p spectra of all samples displayed asymmetrical and broad signals, ascribing to two distinct chemical states S $2p_{1/2}$ and S $2p_{3/2}$ (Fig. 10) [12,55]. The peaks at around 164.0 eV (S $2p_{1/2}$) and 162.7 eV (S $2p_{1/2}$), corresponding to C=S bond, indicated the presence of **HL**^{1}, **HL**^{2}, and **HL**^{3} molecules on the zinc surface after exposure to 0.1 M NaCl solution containing inhibitors [55,64]. Additionally, a shoulder peak around 161.5 - 162.0 eV verified a chemical interaction between S atoms and the zinc surface [55]. This interaction can be attributed to coordination involving the lone pairs of S atoms and the unoccupied outer orbitals of Zn centers. The absence of a signal near 167 eV in the S 2p spectra of all samples further demonstrated that sulfur atoms in the inhibitor molecules were not oxidized during the exposure time.

The O 1 s spectra of all samples exhibited three peaks (Fig. 11). The peak at about 529.4 eV implied O-metal bonds (O–Zn) from zinc oxide [55,65]. The main O 1 s peak, located around 532.0 eV, was assigned to hydroxide groups originating from zinc hydroxide or adsorbed water molecules [65]. A third peak at approximately 534.0 eV was related to O–C bonds [66].

In the Zn $2p_{3/2}$ spectra, two peaks at around 1021.5 eV and 1022.5 eV belonging to Zn–O bonds of zinc oxide and Zn–OH bonds of zinc hydroxide, respectively, indicated the formation of a $ZnO/Zn(OH)_2$ mixture on the zinc surface (Fig. 12) [56,65]. In addition, Zn LMM Auger spectra were employed for a more in-depth examination of the oxidation state of zinc on the surface of all samples (Fig. 13). The peak at around 494.5 eV was attributed to metallic zinc and/or zinc in a low oxidation state, essentially close to Zn(0) [55,67]. Peaks at higher binding energy were due to oxidized zinc species (Zn(II)) [67]. The $ZnO/Zn(OH)_2$ formation on zinc surface in chloride solution could account for the main peak at around 498.0-498.5 eV [55,68]. A shoulder observed around 500.0 eV, exhibiting a higher binding energy than the zinc oxide peak, has also been reported in previous studies. It was showed that the ZnO peak shifts toward higher binding energy in electrolyte solutions containing organic compounds [7,57,68]. Based on the N 1 s and S 2p spectra, the shoulder at around 500.0 eV detected after immersion in the **HL**-containing solutions may be associated with the interaction between zinc and/or zinc oxide with **HL** molecules, resulting in the formation of Zn(II)(**HL**)$_n$ complexes.

3.4. DFT calculations

Additional theoretical studies were performed to elucidate the

nature of the inhibitor-metal interactions and to clarify the reactivity trends among **HL^1**, **HL^2**, and **HL^3**. Although gas-phase optimization of **HL^2** indicated that the *syn* conformation is more stable than the *anti* form, it is noteworthy that, for **HL^2** and analogous acyl thiosemicarbazides containing potential donor atom(s) within the acyl moiety, the *anti* isomer is typically responsible for coordination with transition metal ions, leading to the formation of stable metal complexes [23,51,69]. Therefore, the *anti* conformations of **HL^1**, **HL^2**, and **HL^3** were considered in subsequent studies. The electron distribution and reactive regions of the isolated organic compounds were analyzed using frontier molecular orbital (FMO) and molecular electrostatic potential (MEP) analyses. The HOMOs (Fig. S11) were mainly localized on the sulfur atoms, which explains the negligible variation in HOMO energy across the three compounds regardless of the substituent groups. In contrast, the LUMOs (Fig. S11) are localized on the functionalized aromatic rings, and their energy increased in the order **HL^1** < **HL^2** < **HL^3**, in accordance with the electron-donating strength of the substituents (–OH in **HL^2** and –NH_2 in **HL^3**). Since the inhibitors act as electron donors toward the metal surface, the shape and energy of the HOMO are particularly relevant. The similarity in HOMO energies among the three molecules suggests that the distinctive inhibition performance of **HL^3** does not originate from inherent features of the isolated molecules.

MEP calculations performed at both finite and periodic DFT levels yielded consistent results, showing electron-rich regions (red) localized on the carbonyl and thiocarbonyl moieties (Fig. 14). Notably, the contrast between electron-rich (red) and electron-poor (blue) regions was more pronounced for **HL^3**, which can be correlated with its higher reactivity.

Electrochemical measurements and surface characterization strongly suggested robust zinc-inhibitor interactions at the metal/oxide-solution interface. From a molecular perspective, such strong interactions can be attributed to charge transfer from the electron-rich moieties of **HL** molecules to the Zn/ZnO surface, that is, an electrophilic attack from the surface. The electrophilic Fukui ($f^{(-)}$) indices (Table S4, S5, and S6) further supported this interpretation, indicating that the reaction primarily involves the sulfur atom, which displays by far the largest $f^{(-)}$ value (Fig. 15). This observation is consistent with the localization of the HOMO (Fig. S11) on the sulfur atom, which acts as the main electron reservoir of the **HL** compounds. The three principal reactive sites were identified as: (a) the sulfur atom, (b) the *para* carbon atom of the phenyl ring, and (c) the nitrogen atom of the thioamide group. Interestingly, **HL^3** exhibited larger $f^{(-)}$ indices around both the heteroatom substituent on the phenylene ring (position (e)) and its *para* carbon atom (position (d)). These features likely enable both aromatic rings and the heteroatom of **HL^3** to interact more effectively with the surface compared to **HL^1** and **HL^2**.

In addition to analyzing the electronic structures of the inhibitors, their interaction with zinc and zinc oxide surfaces was also investigated at the theoretical level using the computational methodology outlined in Fig. S12 and S13. The adsorption energy was computed on the relaxed **HL**/ZnO and **HL**/Zn interfaces according to the following equation:

$$E_{ads} = E_{HL/surf} - \left(E_{HL} + E_{surf}\right)$$

where $E_{HL/surf}$ is the total energy of the interface, and E_{HL} and E_{surf} are the total energy of the isolated molecule and surface, respectively, in their interface geometries.

The three acyl thiosemicarbazides **HL** show similar adsorption energies on the zinc surface with values of –2.01, –2.20, and –2.24 eV for **HL^1**, **HL^2**, and **HL^3**, respectively. These results confirmed the interaction of the inhibitors and their anchoring on the surface, which was suggested by the EDS analysis. The anchoring strength has been also evaluated by computing the summation of bond order (SBO), i.e. the sum of bond order for all atomic pairs involving one atom of the molecule and one atom of the surface. In the case of adsorption on zinc, the SBO reaches a value close to 2 for all cases. A deeper gaze into atomic contributions revealed a significant contribution of S-Zn pairs, reflecting the strong interaction between sulfur atoms and the top-layer zinc atoms, as also evidenced by XPS measurements. Indeed, the Zn atom interacting with sulfur atom was shifted upward by about 0.5 Å along the *z*-axis relative to the surface plane. Carbon atoms also contributed considerably to the SBO. In this case, no specific bonds formed, but a significant overlap occurred between the aromatic carbon rings and the top Zn atoms. Interestingly, **HL^3**, which is the compound presenting the best corrosion inhibition properties, showed a different SBO contribution profile compared with **HL^1** and **HL^2** (Table 4). The discrimination between **HL^3** and **HL^1**/**HL^2** became even more significant when considering the oxidized zinc surface (modeled as pure ZnO). Moving from a pure metal to a pure oxide surface induces only a modest variation in the adsorption energy (0.20-0.25 eV) for **HL^1** and **HL^2**, while **HL^3** displayed a substantial increase of 1.3 eV, indicating stronger anchoring. For **HL^1** and **HL^2**, the contribution of carbon atoms to the SBO decreased by nearly 50%, while **HL^3** showed the opposite trend. Meanwhile, the contribution of sulfur atoms to the SBO became negligible for all compounds and did not play any role in anchoring on the oxide surface. Based on those results, the superior inhibitor properties of **HL^3** compared with **HL^2** and **HL^1** may be attributed to its enhanced anchoring ability when the metal surface starts to be oxidized. This property enables **HL^3** to form a more stable protective film which prevents the surface for further corrosion.

The projected density of states (PDOS) of the **HL**/ZnO interfaces was also examined, as these systems displayed a large variation in the amplitude of charge transfer (Fig. 16). It is interesting that in the case of **HL^3**, the HOMO level was found to align with the valence band of ZnO, a feature not perceived for **HL^1** and **HL^2**. This alignment correlates with a shorter interfacial separation, which promotes stronger hybridization between the orbitals of **HL^3** and those of the oxide (Table S7). These results strongly support the higher adsorption energy and bond order values obtained for **HL^3** compared to **HL^1** and **HL^2** (Table 4).

3.5. Discussion

Immersion of zinc substrate in saline solution initiates zinc dissolution, as shown in Eq. (1) [2]. Simultaneously, the cathodic reaction involves oxygen reduction (Eq. (2)) [2,59]. The resulting Zn^{2+} ions subsequently react with OH^- ions to form precipitates such as $Zn(OH)_2$ and ZnO (Eq. (3) and (4)) [2,59]. However, previous studies have reported that ZnO formed in NaCl solution contains numerous defects and large voids, which significantly reduce its corrosion resistance. Therefore, a marked decrease in $|Z|_{10\ mHz}$ and R_{ct} values was observed for zinc after 24 h exposure to saline solution (Table 2).

$$Zn \rightarrow Zn^{2+} + 2\ e^- \quad (1)$$

$$O_2 + 4e^- + 2H_2O \rightarrow 4OH^- \quad (2)$$

$$Zn^{2+} + 2OH^- \rightarrow Zn(OH)_2 \quad (3)$$

$$Zn(OH)_2 \rightarrow ZnO + H_2O \quad (4)$$

All three candidates exhibited inhibitory activity against the short-term corrosion of zinc substrates in the chloride-containing environment. XPS and EDS analyses confirmed that the protective films formed through coordination between the N, O, and S donor atoms of the inhibitor molecules and Zn^{2+} ions. The complex formation mechanism likely involves hydroxide species generated in the cathodic region via oxygen reduction (Eq. 2), which subsequently react with the organic inhibitors. Specifically, deprotonation of the hydrazide NH groups yielded $\{\mathbf{L}\}^-$ and $\{\mathbf{L}\}^{2-}$ anions, which then coordinated with Zn^{2+} centers to form stable complexes [23,51]. The resulting coordination complexes were anchored onto the native oxide layer, thereby reinforcing ZnO stability. These films acted as an additional barrier that suppressed chloride ion penetration into the underlying zinc surface

beneath the $ZnO/Zn(OH)_2$ layers, ultimately enhancing corrosion resistance [55].

Noticeably, EIS results demonstrated that all three inhibitors improved the corrosion resistance of zinc in NaCl solution, with comparable impedance values during the first 6 h (Table 2). However, after 24 h, **HL^3** clearly outperformed **HL^1** and **HL^2** at the same concentration, showing the highest impedance and charge transfer resistance values (Table 2). This behavior can be explained by the DFT studies on the inhibitors in isolated and metal/metal oxide-interacted states. While the three molecules displayed relatively similar adsorption energies on the metallic zinc surface, **HL^3** with pronounced electronic structure exhibited a much stronger anchoring ability on oxidized zinc surfaces (Table 4). This enhanced anchoring promoted the persistence and compactness of the inhibitor film, thereby stabilizing the $ZnO/Zn(OH)_2$ layers and effectively hindering chloride ion penetration. The strong correlation between the EIS observations and the DFT predictions highlighted that the exceptional inhibition performance of **HL^3** originated from its ability to form a more robust and durable interfacial layer once the zinc surface became partially oxidized.

4. Conclusion

This work presents the first systematic investigation of three acyl thiosemicarbazides as corrosion inhibitors for zinc substrate in 0.1 M NaCl solution using electrochemical, surface analyses and thereotical calculations. Polarization curves confirmed that these organic compounds functioned as mixed-type inhibitors with predominant anodic control. The anti-corrosion efficiency of zinc substrate improved with increasing **HL^1** concentration, while at the same concentration, **HL^3** exhibited the strongest inhibitory effect, with the overall order of effectiveness being **HL^3** > **HL^2** > **HL^1**. SEM surface analyses revealed smoother and less damaged zinc surfaces in the presence of the inhibitors, while XPS confirmed the adsorption of inhibitor molecules and their zinc complexes on the surface. These experimental findings were further supported by DFT simulations, which showed that although the three inhibitors exhibited comparable adsorption energies on the metallic zinc surface, **HL^3** with its better electron-donating nature displayed a significantly stronger anchoring ability on the oxidized zinc surface. This enhanced interaction accounts for its superior film stability and long-term inhibition performance observed in EIS. The strong consistency between theoretical predictions and experimental data highlights the decisive role of electronic structure in governing inhibitor efficiency, thereby confirming acyl thiosemicarbazides as promising candidates for zinc protection in neutral chloride media.

Appendix A. Supplementary data

CCDC 2346486 contains the supplementary crystallographic data for compound **HL^2**. The data can be obtained free of charge via http://www.ccdc.cam.ac.uk/conts/retrieving.html, or from the Cambridge Crystallographic Data Center, 12 Union Road, Cambridge CB2 1EZ, UK; fax: +441223 336 033; or e-mail: deposit@ccdc.cam.ac.uk. Supplementary data associated with this article can be found, in the online version, at ….

CRediT authorship contribution statement

Thu Thuy Pham: Writing – original draft, Validation, Methodology, Investigation. **Chien Thang Pham:** Writing – review & editing, Validation, Supervision, Methodology. **Hong Nhung Nguyen:** Validation, Investigation. **Quang Khanh Nguyen:** Validation. **Anh Son Nguyen:** Validation, Investigation. **David Cornil:** Software, Methodology, Investigation. **Jérôme Cornil:** Validation, Supervision, Methodology. **Thuy Duong Nguyen:** Validation, Investigation. **Alice Belfiore:** Validation, Investigation. **Thi Xuan Hang To:** Validation, Supervision, Methodology. **Marie-Georges Olivier:** Writing – review & editing, Supervision, Funding acquisition, Conceptualization.

Declaration of competing interest

The authors declare that they have no known competing financial interests or personal relationships that could have appeared to influence the work reported in this paper.

Acknowledgments

This work was financially supported by the Académie de Recherche et d'Enseignement Supérieur (ARES) through the Development Cooperation project between Vietnam and Belgium (PRD 2020-2025), and, Ministry of Science and Technology (Vietnam) under grant number DTDLCN.61/22. Q. K. N. would like to thank the Hyundai Motor Chung Mong-Koo Foundation for the financial support and global scholarship (FGSS-21-0013) for integrated master-doctoral course at Hanyang University. The theoretical part has been supported by the Fund for Scientific Research (FRS) of FNRS within the Consortium des Equipements de Calcul Intensif (CECI) under grant 2.5020.11 and by the Walloon Region (LUCIA Tier-1 supercomputer; grant number 1910247). J.C. is an FNRS research director.

Supplementary materials

Supplementary material associated with this article can be found, in the online version, at doi:10.1016/j.molstruc.2025.144342.

Data availability

Data will be made available on request.

References

[1] L.B. Coelho, E.B. Fava, A.M. Kooijman, Y. Gonzalez-Garcia, M.G. Olivier, Molybdate as corrosion inhibitor for hot dip galvanised steel scribed to the substrate: A study based on global and localised electrochemical approaches, Corros. Sci. 175 (2020) 108893, https://doi.org/10.1016/j.corsci.2020.108893.

[2] Y. Meng, L. Liu, D. Zhang, C. Dong, Y. Yan, A.A. Volinsky, L.N. Wang, Initial formation of corrosion products on pure zinc in saline solution, Bioact. Mater. 4 (2019) 87–96, https://doi.org/10.1016/j.bioactmat.2018.08.003.

[3] Y. Chen, W. Zhang, M.F. Maitz, M. Chen, H. Zhang, J. Mao, Y. Zhao, N. Huang, G. Wan, Comparative corrosion behavior of Zn with Fe and Mg in the course of immersion degradation in phosphate buffered saline, Corros. Sci. 111 (2016) 541–555, https://doi.org/10.1016/j.corsci.2016.05.039.

[4] J.L. Matos, V. Cerveira, S.M. Manhabosco, S.P.G. Valenzuela, D.P. Dick, L.F.P. Dick, Humic acid: A new corrosion inhibitor of zinc in chlorides, Electrochim. Acta 397 (2021) 139225, https://doi.org/10.1016/j.electacta.2021.139225.

[5] M. Mouanga, P. Berçot, J.Y. Rauch, Comparison of corrosion behaviour of zinc in NaCl and in NaOH solutions. Part I: corrosion layer characterization, Corros. Sci. 52 (2010) 3984–3992, https://doi.org/10.1016/j.corsci.2010.08.003.

[6] N. Macháčková, D. Rudomilova, T. Prošek, G. Luckeneder, Corrosion mechanism of press-hardened steel with zinc coating in controlled atmospheric conditions: A laboratory investigation, Corros. Sci. 240 (2024) 112477, https://doi.org/10.1016/j.corsci.2024.112477.

[7] J. Rodriguez, M. Mouanga, A. Roobroeck, D. Cossement, A. Mirisola, M.G. Olivier, Study of the inhibition ability of benzotriazole on the Zn-Mg coated steel corrosion in chloride electrolyte, Corros. Sci. 132 (2018) 56–67, https://doi.org/10.1016/j.corsci.2017.12.025.

[8] Q. Deng, M. Rafiuddin Jakeria, A. Elbourne, X.-B. Chen, I.S. Cole, Revisiting inhibition stability of 2-mecaptobenzimidazole as corrosion inhibitor against saline corrosive media: A combined in-situ and ex-situ investigation, Appl. Surf. Sci. 681 (2025) 161558, https://doi.org/10.1016/j.apsusc.2024.161558.

[9] X. Wang, J. Liu, M. Jin, Y. Yan, J. Tang, Z. Jin, A review of organic corrosion inhibitors for resistance under chloride attacks in reinforced concrete: background, mechanisms and evaluation methods, Constr. Build. Mater. 433 (2024) 136583, https://doi.org/10.1016/j.conbuildmat.2024.136583.

[10] T.T. Nguyen, C. Arrighi, T.T. Thai, L. Dangreau, M.F. Gonon, A.T. Trinh, M. G. Olivier, Inhibitive effect of the Ce (III) chloride and nitrate on the corrosion resistance of Zn alloyed sacrificial coatings: effect of alloying compounds of the sacrificial layer, Electrochim. Acta 452 (2023) 142296, https://doi.org/10.1016/j.electacta.2023.142296.

[11] A. Hafazeh, A. Balooch, Z.D. Shanbaraki, M. Azadi, Corrosion inhibition of steel in sulphuric acid using Ferula Assa foetida L. extract as an eco-friendly inhibitor: experimental and computational study, Results. Eng. 25 (2025) 103736, https://doi.org/10.1016/j.rineng.2024.103736.

[12] D.K. Kozlica, A. Kokalj, I. Milošev, Synergistic effect of 2-mercaptobenzimidazole and octylphosphonic acid as corrosion inhibitors for copper and aluminium – An electrochemical, XPS, FTIR and DFT study, Corros. Sci. 182 (2021) 109082, https://doi.org/10.1016/j.corsci.2020.109082.

[13] U. Eduok, O. Faye, J. Szpunar, M. Khaled, CS_2 mediated synthesis of corrosion-inhibiting mercaptobenzothiazole molecule for industrial zinc: experimental studies and molecular dynamic simulations, J. Mol. Liq. 324 (2021) 115129, https://doi.org/10.1016/j.molliq.2020.115129.

[14] A.M. Guruprasad, H.P. Sachin, G.A. Swetha, B.M. Prasanna, Corrosion inhibition of zinc in 0.1 M hydrochloric acid medium with clotrimazole: experimental, theoretical and quantum studies, Surf. Interfaces. 19 (2020) 100478, https://doi.org/10.1016/j.surfin.2020.100478.

[15] N. El Hamdani, R. Fdil, M. Tourabi, C. Jama, F. Bentiss, Alkaloids extract of Retama monosperma (L.) Boiss. Seeds used as novel eco-friendly inhibitor for carbon steel corrosion in 1 M HCl solution: electrochemical and surface studies, Appl. Surf. Sci. 357 (2015) 1294–1305, https://doi.org/10.1016/j.apsusc.2015.09.159.

[16] G.E. Badr, The role of some thiosemicarbazide derivatives as corrosion inhibitors for C-steel in acidic media, Corros. Sci. 51 (2009) 2529–2536, https://doi.org/10.1016/j.corsci.2009.06.017.

[17] P. Mohan, G.P. Kalaignan, 1, 4-Bis (2-nitrobenzylidene) thiosemicarbazide as effective corrosion inhibitor for mild steel, J. Mater. Sci. Technol. 29 (2013) 1096–1100, https://doi.org/10.1016/j.jmst.2013.07.006.

[18] A.Y. Musa, A.A.H. Kadhum, A.B. Mohamad, M.S. Takriff, Molecular dynamics and quantum chemical calculation studies on 4,4-dimethyl-3-thiosemicarbazide as corrosion inhibitor in 2.5M H_2SO_4, Mater. Chem. Phys. 129 (2011) 660–665, https://doi.org/10.1016/j.matchemphys.2011.05.010.

[19] S.M. Abd El Haleem, S. Abd El Wanees, E.E. Abd El Aal, A. Farouk, Factors affecting the corrosion behaviour of aluminium in acid solutions. I. Nitrogen and/or sulphur-containing organic compounds as corrosion inhibitors for Al in HCl solutions, Corros. Sci. 68 (2013) 1–13, https://doi.org/10.1016/j.corsci.2012.03.021.

[20] M.M. Singh, R.B. Rastogi, B.N. Upadhyay, M. Yadav, Thiosemicarbazide, phenyl isothiocyanate and their condensation product as corrosion inhibitors of copper in aqueous chloride solutions, Mater. Chem. Phys. 80 (2003) 283–293, https://doi.org/10.1016/S0254-0584(02)00513-8.

[21] Y. Dai, Q. Li, H. Gao, L. Li, F. Chen, F. Luo, S. Zhang, Effects of five additives on electrochemical corrosion behaviours of AZ91D magnesium alloy in sodium chloride solution, Surf. Eng. 27 (2011) 536–543, https://doi.org/10.1179/1743294410Y.0000000025.

[22] A. El-Asmy, K. Ibrahim, M. Bekheit, M. Mostafa, Synthesis and structural studies of Co (II), Ni (II), Cu (II), Zn (II) and Cd (II) chelates derived from semicarbazide and thiosemicarbazide derivatives, J Synthesis Reactivity in Inorganic Metal-Organic Chemistry 15 (1985) 287–300, https://doi.org/10.1080/00945718508059388.

[23] H.H. Nguyen, Q.T. Pham, Q.M. Phung, C.D. Le, T.T. Pham, T.N.O. Pham, C. T. Pham, Syntheses, structures, and biological activities of Pd(II) and Pt(II) complexes with some 1-picolinoyl-4-substituted thiosemicarbazides, J. Mol. Struct. 1269 (2022) 133871, https://doi.org/10.1016/j.molstruc.2022.133871.

[24] Bruker, APEX III, Bruker AXS Inc, Madison, Wisconsin, USA, 2019.

[25] Bruker, SADABS, Bruker AXS Inc, Madison, Wisconsin, USA, 2011.

[26] G. Sheldrick, SHELXT - integrated space-group and crystal-structure determination, Acta Crystallogr. Sect. A 71 (2015) 3–8, https://doi.org/10.1107/S2053273314026370.

[27] G. Sheldrick, Crystal structure refinement with SHELXL, Acta Crystallogr. Sect. C 71 (2015) 3–8, https://doi.org/10.1107/S2053229614024218.

[28] O.V. Dolomanov, L.J. Bourhis, R.J. Gildea, J.A.K. Howard, H. Puschmann, OLEX2: a complete structure solution, refinement and analysis program, J. Appl. Crystallogr. 42 (2009) 339–341, https://doi.org/10.1107/S0021889808042726.

[29] J. Yang, C. Blawert, S.V. Lamaka, K.A. Yasakau, L. Wang, D. Laipple, M. Schieda, S. Di, M.L. Zheludkevich, Corrosion inhibition of pure Mg containing a high level of iron impurity in pH neutral NaCl solution, Corros. Sci. 142 (2018) 222–237, https://doi.org/10.1016/j.corsci.2018.07.027.

[30] A.D. Becke, Density-functional thermochemistry. III. The role of exact exchange, J. Chem. Phys. 98 (1993) 5648–5652, https://doi.org/10.1063/1.464913.

[31] P.J. Stephens, F.J. Devlin, C.F. Chabalowski, M.J. Frisch, Ab initio calculation of vibrational absorption and circular dichroism spectra using density functional force fields, J. Phys. Chem. 98 (1994) 11623–11627, https://doi.org/10.1021/j100096a001.

[32] F. Weigend, R. Ahlrichs, Balanced basis sets of split valence, triple zeta valence and quadruple zeta valence quality for H to Rn: design and assessment of accuracy, Phys. Chem. Chem. Phys. 7 (2005) 3297–3305, https://doi.org/10.1039/B508541A.

[33] S. Grimme, S. Ehrlich, L. Goerigk, Effect of the damping function in dispersion corrected density functional theory, J. Chem. Phys. 32 (2011) 1456–1465, https://doi.org/10.1002/jcc.21759.

[34] F. Neese, F. Wennmohs, U. Becker, C. Riplinger, The ORCA quantum chemistry program package, J. Phys. Chem. 152 (2020) 224108, https://doi.org/10.1063/5.0004608.

[35] M.J. Frisch, G.W. Trucks, H.B. Schlegel, G.E. Scuseria, M.A. Robb, J.R. Cheeseman, G. Scalmani, V. Barone, G.A. Petersson, H. Nakatsuji, X. Li, M. Caricato, A.V. Marenich, J. Bloino, B.G. Janesko, R. Gomperts, B. Mennucci, H.P. Hratchian, J.V. Ortiz, A.F. Izmaylov, J.L. Sonnenberg, Williams, F. Ding, F. Lipparini, F. Egidi, J. Goings, B. Peng, A. Petrone, T. Henderson, D. Ranasinghe, V.G. Zakrzewski, J. Gao, N. Rega, G. Zheng, W. Liang, M. Hada, M. Ehara, K. Toyota, R. Fukuda, J. Hasegawa, M. Ishida, T. Nakajima, Y. Honda, O. Kitao, H. Nakai, T. Vreven, K. Throssell, J.A. Montgomery Jr., J.E. Peralta, F. Ogliaro, M.J. Bearpark, J.J. Heyd, E.N. Brothers, K.N. Kudin, V.N. Staroverov, T.A. Keith, R. Kobayashi, J. Normand, K. Raghavachari, A.P. Rendell, J.C. Burant, S.S. Iyengar, J. Tomasi, M. Cossi, J.M. Millam, M. Klene, C. Adamo, R. Cammi, J.W. Ochterski, R.L. Martin, K. Morokuma, O. Farkas, J.B. Foresman, D.J. Fox *Gaussian 16 Rev. C.01*, Wallingford, CT, 2016.

[36] G. Kresse, J. Furthmuller, Efficient iterative schemes for ab initio total-energy calculations using a plane-wave basis set, Phys. Rev. B 54 (1996) 11169–11186, https://doi.org/10.1103/PhysRevB.54.11169.

[37] G. Kresse, D. Joubert, From ultrasoft pseudopotentials to the projector augmented-wave method, Phys. Rev. B 59 (1999) 1758, https://doi.org/10.1103/PhysRevB.59.1758.

[38] J. Sánchez-Márquez, D. Zorrilla, A. Sánchez-Coronilla, D.M. de los Santos, J. Navas, C. Fernández-Lorenzo, R. Alcántara, J. Martín-Calleja, Introducing "UCA-FUKUI" software: reactivity-index calculations, J. Mol. Model. 20 (2014) 2492, https://doi.org/10.1007/s00894-014-2492-1.

[39] T.A. Manz, N.G. Limas, Introducing DDEC6 atomic population analysis: part 1. Charge partitioning theory and methodology, RSC. Adv. 6 (2016) 47771–47801, https://doi.org/10.1039/C6RA04656H.

[40] N.G. Limas, T.A. Manz, Introducing DDEC6 atomic population analysis: part 2. Computed results for a wide range of periodic and nonperiodic materials, RSC. Adv. 6 (2016) 45727–45747, https://doi.org/10.1039/C6RA05507A.

[41] A.A. El-Asmy, T.Y. Al-Ansi, R.R. Amin, F.M. El-Shahat, Structural studies on cadmium(II), cobalt(II), copper(II), nickel(II) and zinc(II) complexes of 1-malonyl-bis(4-phenylthiosemicarbazide), Transit. Met. Chem 15 (1990) 12–15, https://doi.org/10.1007/bf01032222.

[42] N.M. Hosny, H.M. Mahmoud, M.H. Abdel-Rhman, Spectral, optical, and cytotoxicity studies on N-(2-isonicotinoylhydrazine-carbonothioyl)benzamide and its metal complexes, Heteroat. Chem 29 (2018) e21415, https://doi.org/10.1002/hc.21415.

[43] T.A. Fayed, M. Gaber, G.M. Abu El-Reash, M.M. El-Gamil, Structural, DFT/B3LYP and molecular docking studies of binuclear thiosemicarbazide Copper (II) complexes and their biological investigations, Appl. Organomet. Chem. 34 (2020) e5800, https://doi.org/10.1002/aoc.5800.

[44] N.M. Hosny, M.A. Hussien, R. Motawa, A. Belal, M.H. Abdel-Rhman, Synthesis, spectral, modeling, docking and cytotoxicity studies on 2-(2-aminobenzoyl)-N-ethylhydrazine-1-carbothioamide and its divalent metal complexes, Appl. Organomet. Chem. 34 (2020) e5922, https://doi.org/10.1002/aoc.5922.

[45] O.A. El-Gammal, M.A. El-Nawawy, H.A. Gomaa, B.M. Ismael, Synthesis, spectral, DFT, intrinsic constant of DNA binding and antioxidant activity of vanadyl (IV)2+ complexes of a symmetrical bisthiosemicarbazides, J. Mol. Struct. 1284 (2023) 135335, https://doi.org/10.1016/j.molstruc.2023.135335.

[46] A. Ameryckx, L. Thabault, L. Pochet, S. Leimanis, J.H. Poupaert, J. Wouters, B. Joris, F. Van Bambeke, R. Frédérick, 1-(2-Hydroxybenzoyl)-thiosemicarbazides are promising antimicrobial agents targeting d-alanine-d-alanine ligase in bacterio, Eur. J. Med. Chem. 159 (2018) 324–338, https://doi.org/10.1016/j.ejmech.2018.09.067.

[47] A. Ameryckx, L. Pochet, G. Wang, E. Yildiz, B.E. Saadi, J. Wouters, F. Van Bambeke, R. Frédérick, Pharmacomodulations of the benzoyl-thiosemicarbazide scaffold reveal antimicrobial agents targeting d-alanyl-d-alanine ligase in bacterio, Eur. J. Med. Chem. 200 (2020) 112444, https://doi.org/10.1016/j.ejmech.2020.112444.

[48] R.N. Gautam, A. Tiwari, S. Gupta, M.K. Bharty, V. Ganesan, S. Kumar, P. Bharati, R. J. Butcher, Mn(II) complexes of 1-(4-methoxybenzoyl)-4-phenyl-3-thiosemicarbazide containing o-phenanthroline and 2,2-bipyridine as co-ligands: synthesis, crystal structure, spectral characterization, photoluminescence and electrochemical studies, J. Mol. Struct. 1278 (2023) 134907, https://doi.org/10.1016/j.molstruc.2023.134907.

[49] R.N. Gautam, A. Shukla, S. Chandra, S. Kumar, A. Acharya, M. Singh, R.J. Butcher, M.K. Bharty, Anticancer evaluation of Co(III) complex derived from 1-isonicotinoyl-4-(4-nitrophenyl)-3-thiosemicarbazide: structural characterization, photophysical, and Hirshfeld studies, Inorg. Chem. Commun. 171 (2025) 113521, https://doi.org/10.1016/j.inoche.2024.113521.

[50] M. Pitucha, Z. Karczmarzyk, M. Swatko-Ossor, W. Wysocki, M. Wos, K. Chudzik, G. Ginalska, A. Fruzinski, Synthesis, In vitro screening and docking studies of new thiosemicarbazide derivatives as antitubercular agents, Molecules. 24 (2019) 251, https://doi.org/10.3390/molecules24020251.

[51] H.H. Nguyen, T.T. Pham, N.O. Pham-Thi, V.H. Tran, C.D. Le, B. Van Hoi, T. N. Trieu, C.T. Pham, Syntheses, structures, and anticancer activities of a series of trinuclear Cu(II) complexes with N-methylanthraniloyl(4-phenylthiosemicarbazide), J. Mol. Struct. 1249 (2022) 131680, https://doi.org/10.1016/j.molstruc.2021.131680.

[52] H.P.G. Thompson, G.M. Day, Which conformations make stable crystal structures? Mapping crystalline molecular geometries to the conformational energy landscape, Chem. Sci. 5 (2014) 3173–3182, https://doi.org/10.1039/C4SC01132E.

[53] T.T. Pham, T.D. Nguyen, A.S. Nguyen, M. Gonon, A. Belfiore, Y. Paint, T.X. Hang To, M.-G. Olivier, Influence of solution pH on the structure formation and protection properties of ZnAlCe hydrotalcites layers on hot-dip galvanized steel, Surf. Coat. Technol. 472 (2023) 129918, https://doi.org/10.1016/j.surfcoat.2023.129918.

[54] J. Wang, J. Zhao, M. Tabish, F. Shi, Q. Cheng, L. Peng, Protection of Zn Mg Al coated steel corrosion by cerium gluconate in 0.05 M NaCl solution, J. Mol. Liq. 361 (2022) 119595, https://doi.org/10.1016/j.molliq.2022.119595.

[55] Q. Deng, S. Jeschke, B.J. Murdoch, S. Hirth, P. Eiden, J.N. Gorges, P. Keil, X.-B. Chen, I. Cole, In-depth insights of inhibitory behaviour of 2-amino-4-methyl-thiazole towards galvanised steel in neutral NaCl solution, Corros. Sci. 199 (2022) 110206, https://doi.org/10.1016/j.corsci.2022.110206.

[56] J.M. Ferreira, K.P. Souza, F.M. Queiroz, I. Costa, C.R. Tomachuk, Electrochemical and chemical characterization of electrodeposited zinc surface exposed to new

surface treatments, Surf. Coat. Technol. 294 (2016) 36–46, https://doi.org/10.1016/j.surfcoat.2016.03.023.
[57] T. Kosec, I. Milošev, B. Pihlar, Benzotriazole as an inhibitor of brass corrosion in chloride solution, Appl. Surf. Sci. 253 (2007) 8863–8873, https://doi.org/10.1016/j.apsusc.2007.04.083.
[58] K. Hu, J. Zhuang, J. Ding, Z. Ma, F. Wang, X. Zeng, Influence of biomacromolecule DNA corrosion inhibitor on carbon steel, Corros. Sci. 125 (2017) 68–76, https://doi.org/10.1016/j.corsci.2017.06.004.
[59] I.A. Kartsonakis, S.G. Stanciu, A.A. Matei, R. Hristu, A. Karantonis, C.A. Charitidis, A comparative study of corrosion inhibitors on hot-dip galvanized steel, Corros. Sci. 112 (2016) 289–307, https://doi.org/10.1016/j.corsci.2016.07.030.
[60] H. Wang, T. He, D. Quan, T. Wang, C. Li, Y. Shen, Thiosemicarbazide-linked covalent organic framework: preparation, properties and applications, ChemistrySelect. 6 (2021) 11490–11495, https://doi.org/10.1002/slct.202103227.
[61] R. Sitko, M. Musielak, M. Serda, E. Talik, B. Zawisza, A. Gagor, M. Malecka, Thiosemicarbazide-grafted graphene oxide as superior adsorbent for highly efficient and selective removal of mercury ions from water, Sep. Purif. Technol. 254 (2021) 117606, https://doi.org/10.1016/j.seppur.2020.117606.
[62] M. Li, Z. Zhang, R. Li, J.J. Wang, A. Ali, Removal of Pb(II) and Cd(II) ions from aqueous solution by thiosemicarbazide modified chitosan, Int. J. Biol. Macromol. 86 (2016) 876–884, https://doi.org/10.1016/j.ijbiomac.2016.02.027.
[63] J. He, Y. Lu, G. Luo, Ca(II) imprinted chitosan microspheres: an effective and green adsorbent for the removal of Cu(II), Cd(II) and Pb(II) from aqueous solutions, Chem. Eng. J. 244 (2014) 202–208, https://doi.org/10.1016/j.cej.2014.01.096.
[64] V. Garg, S. Zanna, A. Seyeux, F. Wiame, V. Maurice, P. Marcus, Inhibition of the initial stages of corrosion by 2-mercaptobenzothiazole adsorption and the effects of interfacial oxides on copper in neutral chloride conditions, Corros. Sci. 225 (2023) 111596, https://doi.org/10.1016/j.corsci.2023.111596.
[65] Z. Chen, X. Liu, Z. Cheng, X. Tan, Y. Xiang, J. Li, Y. Zhang, Z. Lu, E.-T. Kang, L. Xu, X. Rao, Degradation behavior, biocompatibility and antibacterial activity of plasma electrolytic oxidation treated zinc substrates, Surf. Coat. Technol. 455 (2023) 129234, https://doi.org/10.1016/j.surfcoat.2023.129234.
[66] M. Ahmad, K. Manzoor, S. Ahmad, S. Ikram, Retraction of "preparation, kinetics, thermodynamics, and mechanism evaluation of thiosemicarbazide modified green carboxymethyl cellulose as an efficient Cu(II) adsorbent, J. Chem. Eng. Data 65 (2019) 939, https://doi.org/10.1021/acs.jced.7b01008, 939.
[67] J. Rodriguez, L. Chenoy, A. Roobroeck, S. Godet, M.G. Olivier, Effect of the electrolyte pH on the corrosion mechanisms of Zn-Mg coated steel, Corros. Sci. 108 (2016) 47–59, https://doi.org/10.1016/j.corsci.2016.02.041.
[68] L.P. Kazansky, Y.E. Pronin, I.A. Arkhipushkin, XPS study of adsorption of 2-mercaptobenzothiazole on a brass surface, Corros. Sci. 89 (2014) 21–29, https://doi.org/10.1016/j.corsci.2014.07.055.
[69] K.-K. Du, S.-X. Liu, Influence of pH values on the self-assembly in three trinuclear nickel complexes with bridging ligand *N*-salicylyl 4-phenyl-thiosemicarbazide, J. Mol. Struct. 874 (2008) 138–144, https://doi.org/10.1016/j.molstruc.2007.03.048.